Nitrogen-defect-modified g-C₃N₄/BaFe₁₂O₁₉ S-scheme heterojunction photocatalyst with enhanced advanced oxidation technology synergistic photothermal degradation ability of antibiotic: Insights into performance, electron transfer pathways and toxicity

Puyang Zhou, Yan Wang, Xiaorui Yan, Yu Gan, Changkun Xia, Yuanguo Xu [*], Meng Xie [**]

School of Chemistry and Chemical Engineering, School of Pharmacy, Jiangsu University, Zhenjiang 212013, PR China

ARTICLE INFO

ABSTRACT

In this research, nitrogen-defect-modified g-C₃N₄/BaFe₁₂O₁₉ S-scheme heterojunction composites were prepared by in-situ thermal polymerization approach and employed as a productive photo-Fenton catalyst for degrading antibiotic. The micromorphology, crystal structure, chemical composition and optical characteristics of the photocatalysts were evaluated by various testing approaches. The formation of the internal electric field between g-C₃N₄ and BaFe₁₂O₁₉ and the construction of the S-scheme heterojunction were confirmed by density functional theory and Kelvin probe force microscopy. Meanwhile, the nitrogen defect and photothermal effect of the g-C₃N₄/BaFe₁₂O₁₉ composite further accelerate the electron migration rate. The optimized g-C₃N₄/BaFe₁₂O₁₉-30 photocatalyst achieved 100% enrofloxacin removal within 10 min compared to monomer g-C₃N₄. The bactericidal activity experiment showed that the photocatalytic degradation products were low or non-toxic. Based on the above characterization experiments and density functional theory, the possible degradation mechanism of enrofloxacin was proposed. This research offers new insights for the synthesis of photocatalyst for wastewater treatment.

1. Introduction

At present, the synthetic third-generation fluoroquinolone enrofloxacin (ENR) is often used for respiratory and digestive tract infections in animals. However, ENR is not completely digested, and more than half of consumed medication doses are eliminated in urine or feces [1]. Unfortunately, ENR has a low biodegradability, and traditional wastewater treatment systems have limited removal capacity. The concentration of a large number of antibiotics in water has caused serious environmental pollution. Furthermore, long-term consumption of foods with ENR residues can lead to resistance to fluoroquinolone antibiotics. Therefore, it is a critical requirement for the development of a green, efficient, stable and low-cost treatment approach to remove residual antibiotics from aqueous solutions [2].

Advanced oxidant process (AOP) based on H₂O₂, such as Fenton and Fenton-like, have strong oxidizing effects on wastewater treatment. However, the degradation process of Fenton process has some shortcomings that limit its development [3]. For example, the solution requires a strict pH range (pH = 3–5), the production of large quantities of iron mud and low H₂O₂ utilization. Therefore, the multiphase Fenton technique that utilizes solid phase catalysts has been developed for wastewater treatment. Nevertheless, the Fenton system still has the deficiency of low mineralization rate [4]. At present, the introduction of photocatalytic process in polyphase Fenton has received extensive attention [5,6]. In the photo-Fenton process, electrons produced by materials can promote the decomposition of H₂O₂ and the regrowth of Fe²⁺. In particular, since the photo-Fenton reaction is not pH-dependent, it has a wide range of potential applications in real wastewater treatment facilities. Despite the many advantages of the photo-Fenton technology, the core of the technology is the photocatalyst. As a result, developing photocatalysts with high photocatalytic activity for wastewater treatment remains a significant challenge.

As a graphitic non-metallic semiconductor with visible light response, carbon nitride (g-C₃N₄) is commonly used in catalysis because
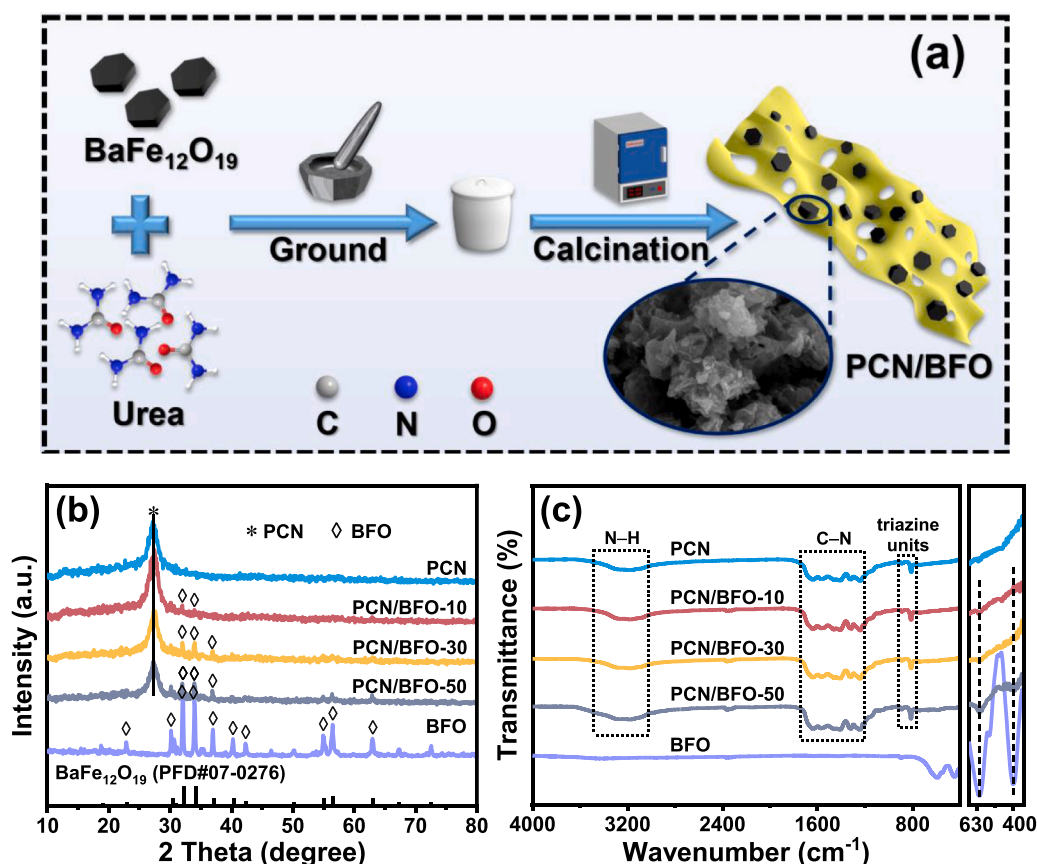

Fig. 1. (a) The diagrams depict the PCN/BFO synthesis process; (b) The XRD patterns and (c) FT-IR spectroscopy of PCN, BFO and PCN/BFO samples.

of its advantages of low cost, high stability and harmless [4,7]. However, the activity of pure g-C_3N_4 in the field of photo-Fenton is still unsatisfactory due to its low band value and high electron hole pair recombination rate. Therefore, modification methods such as element doping [8–10], heterostructure construction [11–13] and defect engineering [14] have been widely used to enhance the photo-Fenton performance of g-C_3N_4. Among them, the introduction of defect sites is an important method to regulate photocatalytic activity. Zhan et al. [15] showed that nitrogen vacancy can broaden visible light absorption and hinder e^--h^+ pairs recombination, thus improving the degradation performance of tetracycline. Wei et al. [16] synthesized C_3N_4 with nitrogen vacancy and cyanide double defect sites. The electron rich structure can improve the carrier separation and light absorption capacity. It showed excellent photodegradability to various PPCPs. However, the single-component materials still have some disadvantages, such as low photo-generated carrier lifetime and insufficient oxidation-reduction capacity.

At the moment, the construction of heterogeneous links is the most prospective strategy [17,18]. The traditional type I or II heterojunction can promote the separation of photogenerated charges, but it sacrifices the reduction and oxidation capacity of the conduction and valence band of the material. Compared with traditional type I or II heterojunctions, S-scheme heterojunctions with strong redox capacity have received a lot of attention in the area of photocatalysis [19–21]. The S-scheme heterojunction is a combination of two semiconductors that have energy band interleaving. Because the work functions of the two materials are different, the internal electric field (IEF) is formed at the interfaces. Band bending caused by the IEF can accelerate the recombination of unwanted electron holes and prolong the carrier lifetime [22, 23]. Therefore, the selection of materials for constructing S-scheme heterojunction semiconductors with g-C_3N_4 is of great significance for enhancing photocatalytic degradation performance. Barium hexaferrite (BaFe$_{12}$O$_{19}$) has come under more and more scrutiny due to its

inexpensive price, strong saturation magnetization, suitable bandgap and chemical stability [24,25]. Xie et al. [26] created a variety of BaFe$_{12}$O$_{19}$/AgBr magnetic reusable hybrids that photodegrade 98.2% of 2–Mercaptobenzothiazole within 30 min. Feng et al. [27] prepared a novel SrTiO$_3$/BaFe$_{12}$O$_{19}$ heterojunction with excellent tetracycline degradation performance by activating PMS. However, the low band value of monomer BaFe$_{12}$O$_{19}$ results in carrier recombination. Therefore, it is a good solution to construct heterojunctions with other materials.

Our research group previously proposed a photocatalyst BaFe$_{12}$O$_{19}$/g-C_3N_4 based on traditional type II heterojunction [28]. However, with the improvement of understanding of photogenerated carrier transfer, the construction of S-scheme heterojunction seems to be more suitable for BaFe$_{12}$O$_{19}$/g-C_3N_4. Firstly, g-C_3N_4 is a highly efficient reducing photocatalyst with a minimum conduction band of − 1.31 eV. At the same time, BaFe$_{12}$O$_{19}$ has a strong oxidizing photocatalyst and its valence band value is up to 2.15 eV. Therefore, the photogenerated e^- and h^+ gather in the high conduction band position of g-C_3N_4 and the low valence band position of BaFe$_{12}$O$_{19}$ respectively, which greatly enhances the redox capacity of the material. Secondly, Fermi level energy is calculated by density functional theory (DFT), as illustrated in Fig. 10. The calculated work functions of g-C_3N_4 and BaFe$_{12}$O$_{19}$ are 4.82 and 5.39 eV, respectively. In order to balance the Fermi level and build an S-scheme heterojunction, electrons are transported from g-C_3N_4 to BaFe$_{12}$O$_{19}$ through the interface of g-C_3N_4 when it comes into contact with BaFe$_{12}$O$_{19}$. The transfer of electrons results in the formation of an IEF. Meanwhile, the Kelvin probe force microscope (KPFM) experiment further confirmed the theoretical calculation results. Therefore, the successful construction of an S-scheme by g-C_3N_4 and BaFe$_{12}$O$_{19}$ replaces the previously reported type II heterojunction [28].

Based on the above discussion, the S-scheme heterojunction g-C_3N_4/BaFe$_{12}$O$_{19}$ composite materials were obtained by defect engineering and
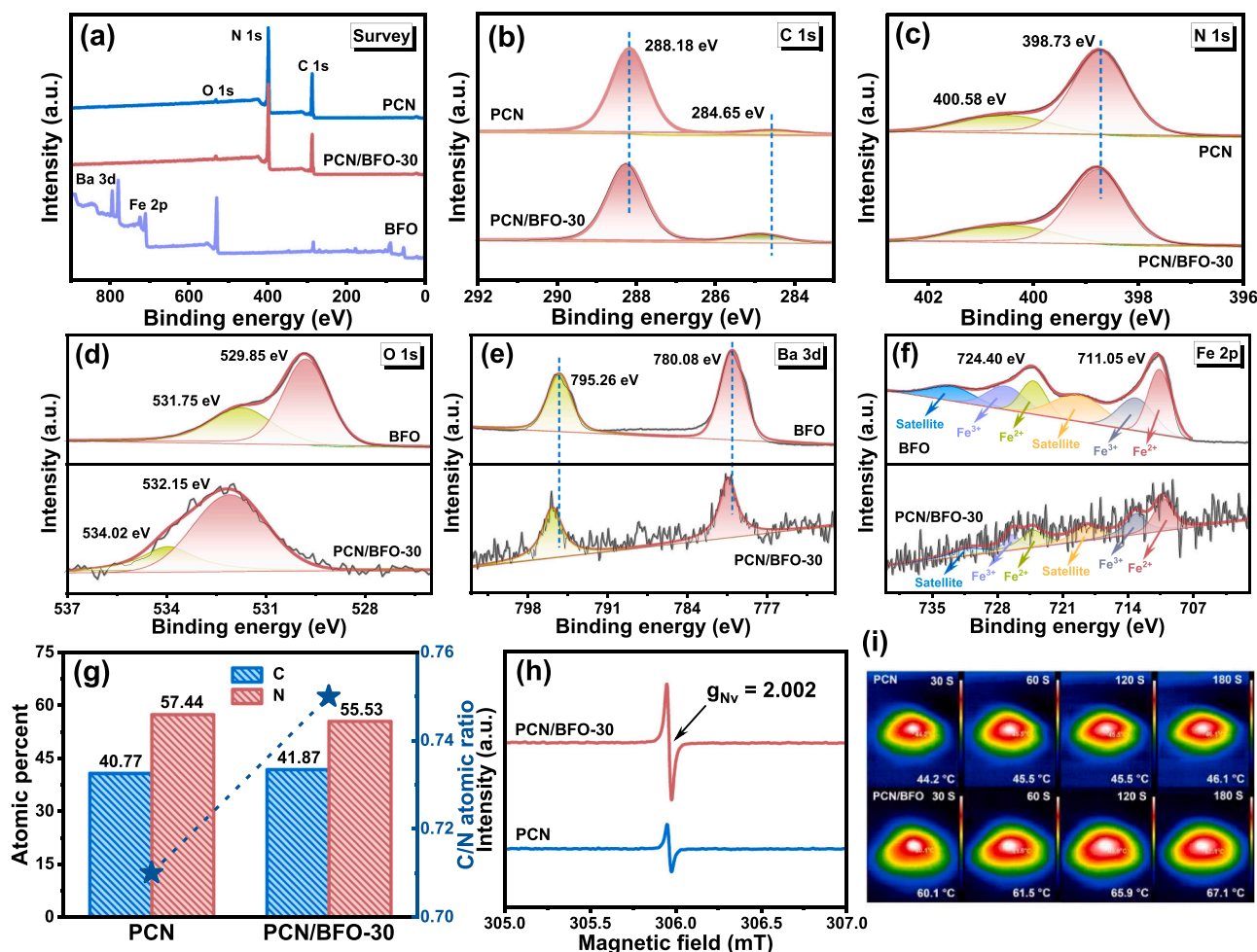
Fig. 2. (a) XPS survey of samples and high-resolution XPS of (b) C 1 s, (c) N 1 s, (d) O 1 s, (e) Ba 3d, and (f) Fe 2p in PCN, BFO and PCN/BFO materials; (g) The ratio of C and N atoms of the sample in the XPS patterns; (h) EPR spectra of PCN and PCN/BFO-30 composites; (i) The IR images of photo-thermal effect for PCN and PCN/BFO-30 powders.

in situ thermal polymerization. The microstructure and electron transfer path of the material were revealed by experimental characterization and theoretical calculation. g-C_3N_4/$BaFe_{12}O_{19}$ materials have excellent electron trapping ability, strong redox performance and significantly promote photogenerated carrier separation. In addition, g-C_3N_4/$BaFe_{12}O_{19}$ photocatalyst has excellent photo-Fenton degradation activity under visible light. The bactericidal activity experiment showed that the degradation products were non-toxic or low toxic. Meanwhile, g-C_3N_4/$BaFe_{12}O_{19}$ demonstrated remarkable cyclic stability and magnetic recovery. Therefore, this study sheds fresh light on the industrial manufacture of S-scheme heterojunction catalysts for environmental cleanup.

2. Experiment

2.1. Materials

The reagents were displayed in the Supplementary Material.

2.2. Synthesis of g-C_3N_4/$BaFe_{12}O_{19}$ photocatalysts

The 10 g urea and 30 mg $BaFe_{12}O_{19}$ are fully ground in agate mortar for at least 15 min, and then put into the crucible and sealed with aluminum foil paper. Calcined in crucible at 550 °C for 2 h (ramp rate of 10 °C/min). The product was named g-C_3N_4/$BaFe_{12}O_{19}$-30 (PCN/BFO-30). The addition of other proportions of $BaFe_{12}O_{19}$ (0, 10 mg, 50 mg) to

the above preparation conditions was named PCN, PCN/BFO-10, and PCN/BFO-50.

2.3. Basic details of light reaction device

The light reaction bottle is made of GG-17 high temperature resistant glass material with light transmittance of 85%. The geometry of the light reaction bottle is similar to the shape of a sandwich cylinder with an opening at the top, and the size of the photoreaction bottle is as follows: length: 215 mm; diameter: 65 mm; volume: 250 mL. The light source is commercial MSD-250(N) xenon lamps. The emission wavelength is 200–1000 nm. The xenon lamp is 60 mm away from the light reaction bottle, and the distance between the xenon lamp and the filter is 30 mm.
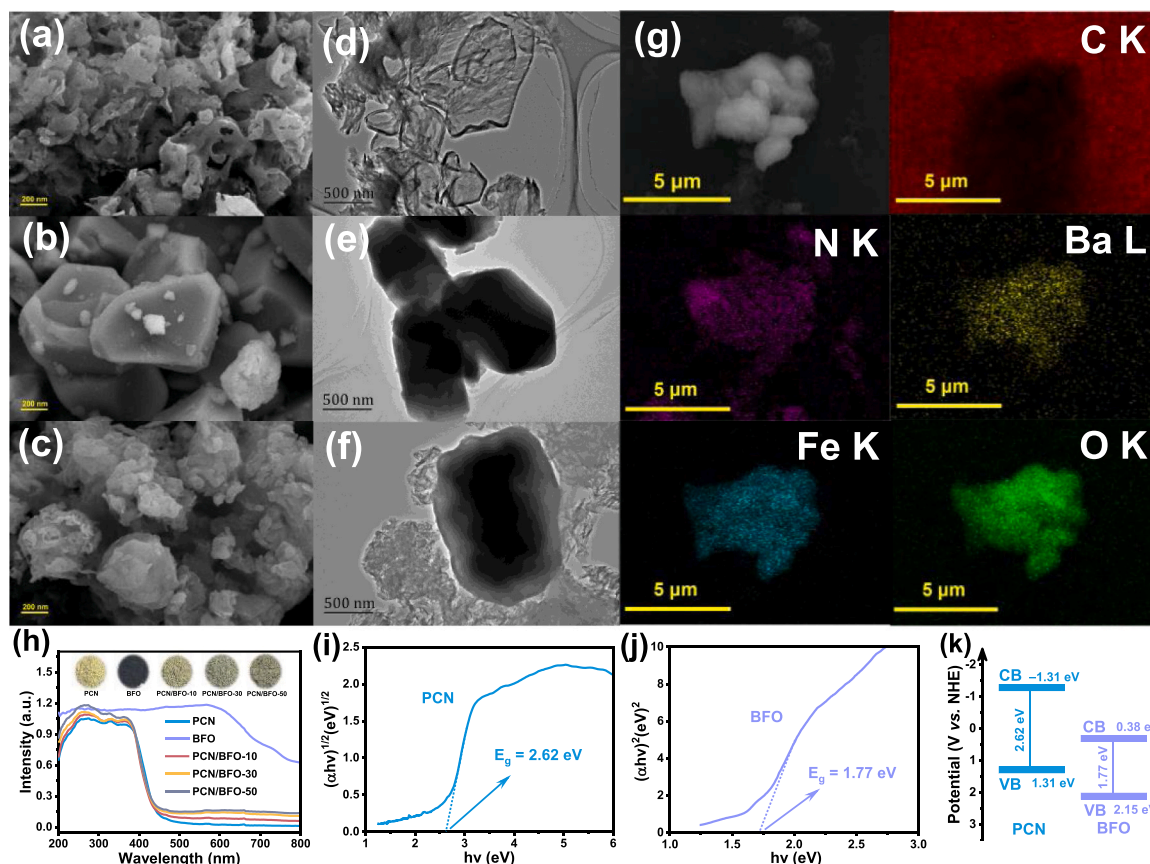
2.4. Characterization, photocatalytic activity tests, antibacterial activities, molecular oxygen activation measurements and calculation method

Details of the information description are reported in the Supplementary Material.

3. Results and discussion

3.1. Microstructure and morphology

A simple one-step grinding and calcination method was used to

Fig. 3. The SEM images of (a) PCN, (b) BFO and (c) PCN/BFO-30; The TEM images of (d) PCN, (e) BFO and (f) PCN/BFO-30; (g) The elemental mapping of PCN/BFO-30; (h) UV–vis diffusion reflectance spectra; Tauc plots of (i) PCN and (j) BFO; (k) Energy band diagram of PCN/BFO materials.

create PCN/BFO composites. Fig. 1a depicts the detailed synthesis procedure. The crystalline structures of PCN, BFO and PCN/BFO were analyzed via XRD measurements. As displayed in Fig. 1b, the XRD pattern of pure PCN (JCPDS 87–1526) shows that the peak at 27.6° belongs to the (002) crystal plane, which are consistent with periodic accumulation of conjugated aromatic system [29]. The typical diffraction peaks of BFO correspond well with the JCPDS 07–0276. Additionally, the peaks of PCN and BFO were all occur in the XRD patterns of the PCN/BFO composites. Meanwhile, the characteristic peaks of BFO are gradually enhanced with the increase of the mass ratio of BFO in the PCN/BFO sample, and the characteristic peak of PCN in composites shifts to a higher angle than that of pure PCN. The results show that the composites are successfully prepared and the carbon nitride layer spacing increases. Interestingly, the peaks of (002) in the composite become sharper and stronger when low content of BFO is introduced, indicating a more ordered structure [30]. The chemical structure of the obtained materials was further studied by FT-IR spectroscopy. It is obvious from the Fig. 1c that the peaks of PCN/BFO composites is highly similar to that of PCN. The broad peak of PCN at $3500 - 3000$ cm^{-1} belongs to the $N - H$ stretching vibration structures [31], and the peaks locating at $1700-1200$ cm^{-1} correlated to the stretching of C–N heterocyclic ring [32]. The tri-s-triazine units have been given the peak at 809 cm^{-1} [33]. Furthermore, there were the absorption peaks at $590–440$ cm^{-1} was observed in pure BFO, which accounted for Ba–O and Fe–O [29]. The characteristic peak of BFO also appeared in PCN/BFO composites, which confirmed the successful preparation of PCN/BFO samples. The results agree well with the XRD analysis.

The chemical state of PCN, BFO and PCN/BFO samples was further analyzed by XPS patterns. As illustrated in Fig. 2a, the survey spectrum shows the presence of C, N and O atoms in PCN/BFO. As revealed in Fig. 2b, the C 1 s spectrum of PCN and PCN/BFO contained two peaks located at 288.18 and 284.65 eV, corresponding to the N $-$ C$=$N bond of sp^2-hybridized carbon and C$-$C bond of carbon delivered with the equipment, respectively [34]. The N 1 s peaks of PCN and PCN/BFO (Fig. 2c) may be deconvoluted to two peaks at 400.58 and 398.73 eV, respectively, reflecting C$-$N $=$ C of sp^2 hybridized nitrogen and N $-$ (C)$_3$ of tertiary nitrogen, respectively [35]. Particularly, the ratio of C$-$N $=$ C to N-C$_3$ fell from 3.46 to 2.91, suggesting that the defects are preferentially engineered at N$_{2 C}$ site. Compared with the binding energy of PCN, it is found that the C and N peaks of PCN/BFO shift to higher binding energy, respectively. This is because the in situ thermal polymerization strategy promotes the tight coupling between PCN and BFO materials [36]. It is also shown that the electron escape on PCN leads to the corresponding increase in binding energy. The O 1 s spectrum of the obtained materials displayed in Fig. 2d. The O 1 s spectra of BFO may be resolved into two peaks contributions located at 531.75 and 529.85 eV, which was consistent with hydroxyl oxygen (OH) and lattice oxygen of BFO, respectively [37]. The peak at 532.15 eV belonged to the lattice oxygen in PCN/BFO. In addition, the XPS spectrum of O 1 s in the PCN/BFO sample is obviously shifted, suggesting the interaction between the materials. Fig. 2e showed the Ba 3d spectrum, the peaks at 795.26 eV (Ba 3d$_{3/2}$) and 780.08 eV (Ba 3d$_{5/2}$) were attributed to the Ba$-$O bond of BFO, respectively [38]. Furthermore, from Fig. 2f, the high-resolution XPS spectrum of Fe 2p deconvoluted to six peaks. Among them, the major peak at 724.40 eV is associated with Fe^{3+} 2p$_{1/2}$ and Fe^{2+} 2p$_{1/2}$, and another major peak at 711.05 eV could be assigned to Fe^{3+} 2p$_{3/2}$ and Fe^{2+} 2p$_{3/2}$. In addition, the peaks at 722.28 and 719.54 eV are satellite peaks of the Fe 2p$_{1/2}$ and Fe 2p$_{3/2}$, respectively [39]. Meanwhile, compared with the Ba 3d and Fe 2p spectrums of PCN, the binding energies of PCN/BFO were all slightly higher, further confirming the successful synthesis of the composites. Compared with PCN, the C/N atom ratio of PCN/BFO composite was increased (from 0.71 to
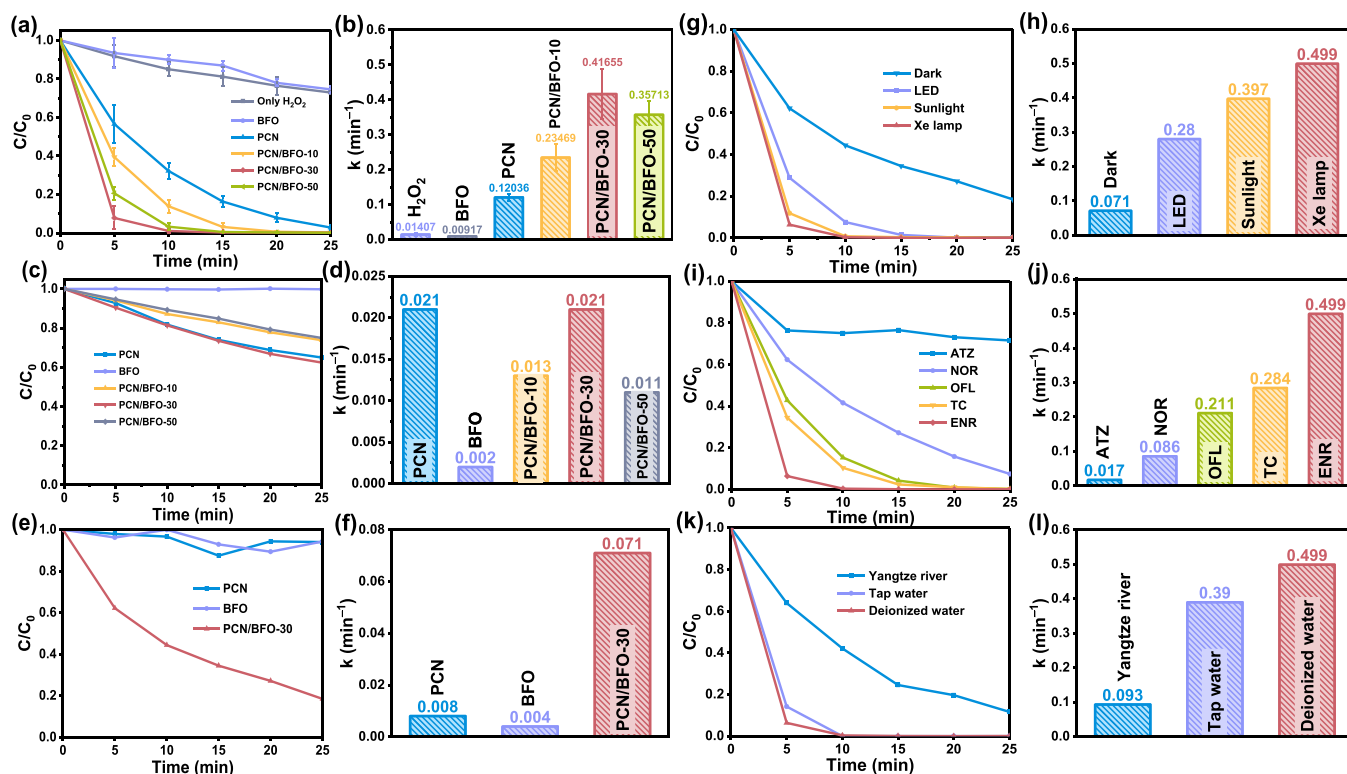
Fig. 4. (a) The photocatalytic degradation efficiency of ENR and (b) photocatalytic kinetic curves of samples; ENR degradation in PCN/BFO system under (c, d) without H_2O_2 and (e, f) without visible light irradiation; The effects of (g, h) different light sources, (i, j) different pollutants and (k, l) different water quality on the degradation performance of photocatalysts.

0.75), indicating that the coupling of BFO promoted the formation of nitrogen defects in the composite (Fig. 2g). In contrast to the original PCN, the PCN/BFO-30 heterostructure showed an increased EPR signal at g = 2.002 (Fig. 2h), which is brought on by unpaired electrons on the carbon atoms of aromatic rings [40]. The production of N defects in PCN/BPO-30 materials is indicated by all of the aforementioned studies. According to the literature [41–43], the introduction of BFO on PCN can enhance the photothermal effect of the composite, and improve the photogenerated carrier separation efficiency of the system. According to the infrared thermal imaging (IR) images in Fig. 2i and S1, it is obvious from the figure that BFO has the strongest photothermal effect. After 30 s of visible light irradiation, the temperature of BFO powder can reach 93.4 °C. With the increase of irradiation time, its temperature can be raised to 147.8 °C after 180 s. Meanwhile, the photothermal effect of PCN/BFO-30 is significantly stronger than that of PCN. Therefore, the S-scheme heterojunction constructed by the photothermal material BFO and PCN can further improve the carrier separation efficiency and reaction system temperature with the help of photothermal.

As depicted in Fig. 3a-g, the morphology and microstructure of PCN, BFO, and PCN/BFO were examined using SEM and TEM. The pure PCN nanosheet has a curly shape made up of narrow folds (Fig. 3a and d). The monomer BFO has a block structure with a diameter of around 500 nm (Fig. 3b and e). As demonstrated in Fig. 3c and f, the SEM image of PCN/ BFO photocatalyst do not clearly demonstrate the successful combination of composite, but the TEM image can clearly observe the coexistence of PCN and BFO. Furthermore, As shown in Fig. S2a, the lattice plane spacing of the BFO in the (114) plane is approximately 0.265 nm. Typical BFO lattice fringes were also found in PCN/BFO, demonstrating that the composite had been properly prepared (Fig. S2b). In addition, the tight contact between PCN and BFO is further confirmed by the PCN/ BFO mapping of EDS elements (C, N, Ba, Fe, and O) (Fig. 3g). When BFO was introduced into PCN, the PCN layer structure in PCN/BPO-30 became thinner (Fig. 3f). In general, ultra-thin nanosheets are more

conducive to carrier migration than other structures, further improving the photocatalytic performance [44]. Meanwhile, aggregation exists in monomer BFO, and the degree of aggregation in PCN/BFO-30 is reduced. The formation of PCN/BFO-30 heterojunction prevents the aggregation of BFO, which improves the carrier separation efficiency and photocatalytic activity [45]. In addition, as can be seen from Fig. 3g and S2b, the tight and uniform contact between PCN and BFO confirms the construction of heterojunction. The construction of heterojunction widened the band gap and inhibited the photogenerated electron hole pair recombination, and further improves the photocatalytic performance [46].

The optical absorption and bandgap structures of obtained samples were measured with UV–vis DRS. As indicated in Fig. 3h, both the ultraviolet and visible light regions of BFO exhibit high absorption, which might be related to color [29]. Color photos of different sample powders are also shown inset in Fig. 3h. The absorption of PCN/BFO photocatalysts in the visible light-absorbing region is gradually enhanced with the increase of BFO content. Furthermore, UV–vis DRS data is transformed into photocatalyst bandgap data via the Kubelka-Munk algorithm [47]. The band gaps of PCN and BFO are 2.62 and 1.77 eV, respectively, as shown in Fig. 3i-j, and these values are consistent with earlier reports [29]. Additionally, the following equation was used to predict the CB and VB positions of pure PCN and BFO materials: $E_{VB} = X - E^C + 0.5\ E_g$, $E_{CB} = E_{VB} - E_g$. Here, X is the electronegativity of the semiconductor (the X values for BFO are 5.77), E^C is the energy of free electrons on the hydrogen scale (4.5 eV). Based on the above calculations and previous reports, the E_{VB} and E_{CB} of PCN were calculated to be 1.31 and − 1.31 eV, respectively, and the corresponding E_{VB} and E_{CB} of BFO were 2.15 and 0.38 eV. The results of this section are shown schematically in Fig. 3k.

3.2. Photocatalytic properties and antibacterial activities

The activity of PCN, BFO and PCN/BFO samples was evaluated by photocatalytic degradation of ENR. As depicted in Fig. 4a, the photocatalytic degradation activity is at its lowest (approximately 25%) when only H_2O_2 are present. Similarly, the ability of pure BFO to activate H_2O_2 is poor. The degrading activity of the defect-mediated materials is greatly improved when the mass of BFO in the composite is raised from 0 to 10 mg and 30 mg, and the corresponding first-order kinetic constant (k) rises from 0.127 to 0.194 and 0.499 min^{-1} (Fig. 4b). When the mass of BFO was increased to 50 mg, its photocatalytic activity slightly decreased (k = 0.399 min^{-1}). This could be owing to an excessive accumulation of BFO, which reduces the active site. Additionally, the obtained materials showed poor degradation activity in the absence of H_2O_2 (Fig. 4c). The activity of PCN/BFO composites is similar to or lower than that of monomer PCN. The cause might be that the insertion of BFO may improve the stability of the composite structure and reduce the compound rate of the electronic hole, hence reducing carrier mobility. The findings are consistent with those reported by Ji et al. and He et al. [48,49]. Furthermore, in order to evaluate the impact of H_2O_2 on the photocatalytic activity of the material, the ability of the material to activate H_2O_2 to degrade pollutants was studied in the dark, as shown in Fig. 4e. Interestingly, both the monomer PCN and BFO were basically inactive, while the catalytic degradation of ENR by PCN/BFO-30 was significantly improved, reaching 80% degradation efficiency after 25 min. In order to investigate the causes for the increased PCN/BFO Fenton reaction activity, ICP-OES was used to measure the metal ion concentration after the degradation reaction (Table S1). The results show that the introduction of PCN can reduce the escape of metal ions and improve the properties of the composites. Moreover, the concentration of Fe ions in the solution did not change significantly, indicating that the reason for the increase in activity should be the combination of PCN and BFO, rather than the circulation of Fe ions in the solution. In addition, the reduction of Ba ions of the composite material in the solution indicates the binding of Ba ions and PCN in BFO. Fig. 4g-h provides an in-depth study of the effects of different light sources (LED, sunlight and Xe lamps) on the degradation performance of photocatalysts. The results show that it has excellent degradation activity under the coordination of visible light irradiation and H_2O_2. Among them, the degradation rate (0.280 min^{-1}) under LED conditions (420 −800 nm) is slightly lower than that of Xe lamps ($\geq$ 420 nm), which may be the reason for the low light intensity. In particular, the photocatalytic performance under sunlight is similar to that of Xe lamps. The outcomes of the experiment demonstrate that the photocatalyst has excellent activity only under sunlight, which further reduces the cost and shows a broad application prospect. Organic pollutants including atrazine (ATZ), norfloxacin (NOR), ofloxacin (OFL), tetracycline (TC), oxytetracycline (OTC), ohlorotetracycline (CTC), ciprofloxacin (CIP) and sulfamethoxazole (SMX) were each degraded in order to investigate the photocatalyst's universality (Fig. 4i-j and S3). The results of the experiments reveal that under the same conditions, the degradation efficiency and rate of different pollutants are ENR (100%, 0.499 min^{-1}) = TC (100%, 0.284 min^{-1}) = OFL (100%, 0.211 min^{-1}) > NOR (92%, 0.086 min^{-1}) > ATZ (22%, 0.017 min^{-1}). PCN/BFO-30 still maintained high degradation activity for OTC, CTC and CIP except for SMX. Its degradation efficiency can be close to 100% after 10 min. Unfortunately, the removal efficiency of PCN/BFO-30 catalysts for SMX is only about 10%. Obviously, the degradation of pesticide pollutants by the material still needs to be further modified and improved. However, it has excellent degradative activity against the most widely used antibiotics. Furthermore, in order to further investigate the activity of photocatalyst for degradation of ENR in different water quality, Yangtze River water, tap water and deionized water were respectively used for degradation experiments (Fig. 4k-l). It can be seen from the experimental results that the photocatalyst also exhibits high degrading activity in tap water. However, the degradation rate (0.093 min^{-1})
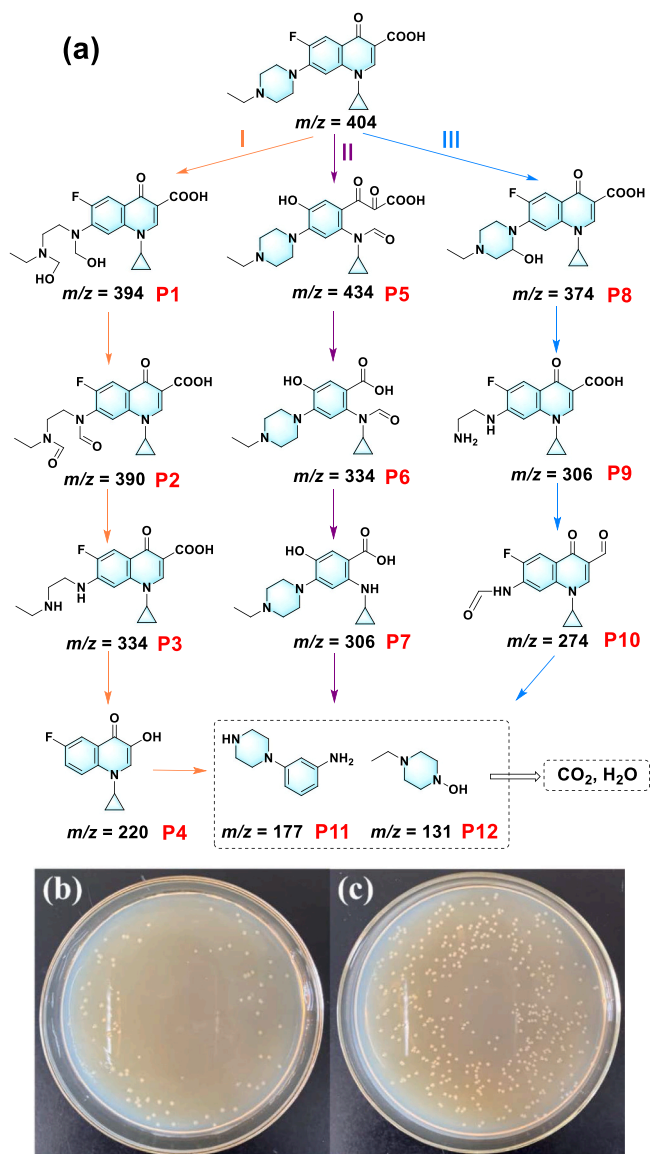
Fig. 5. (a) The proposed photocatalytic degradation pathways; Antibacterial activities of ENR solutions: (b) before and (c) after degradation.

decreased in the Yangtze River water, possibly as a result of the ions in the water and the competitive destruction of organic matter [50].

Based on the Beer-Lambert law [51]: $A = -\lg(I/I_0) = \varepsilon \bullet b \bullet c$. Where A is absorbance, I is the transmitted light intensity, I_0 is the incident light intensity, ε is extinction coefficient, b is optical path length, c is photocatalyst solution concentration. Therefore, the extinction coefficient of the photocatalyst is calculated by the following formula: $\varepsilon = A/(bc) = 2.02/(1\ cm \bullet 1\ mg \bullet mL^{-1}) = 2020\ cm^2/g$. The optical thickness (τ) of the reactor can be calculated by the following formula [51,52]: $\tau = \varepsilon \bullet c \bullet h$. Where c and h represent catalyst concentration and the depth of liquid in reactor, respectively. Therefore, plugging in the data can calculate the optical thickness: $\tau = 2020\ cm^2 \bullet g^{-1} \bullet 1\ mg \bullet mL^{-1} \bullet 1.5\ cm = 3.03$. In general, the optimum optical thickness (τ) in photocatalytic system is 1.8 − 4.4 [52]. Obviously, PCN/BFO-30 composite has the best optical thickness value.

The potential route of photocatalytic degradation of ENR were further analyzed by mass spectrum (Fig. S4 and Fig. 5a). According to speculation, enrofloxacin can break down in three different ways. Piperazine group loss and the division of quinolone components make up the majority of pathway I. First, the piperazine group was epoxidized
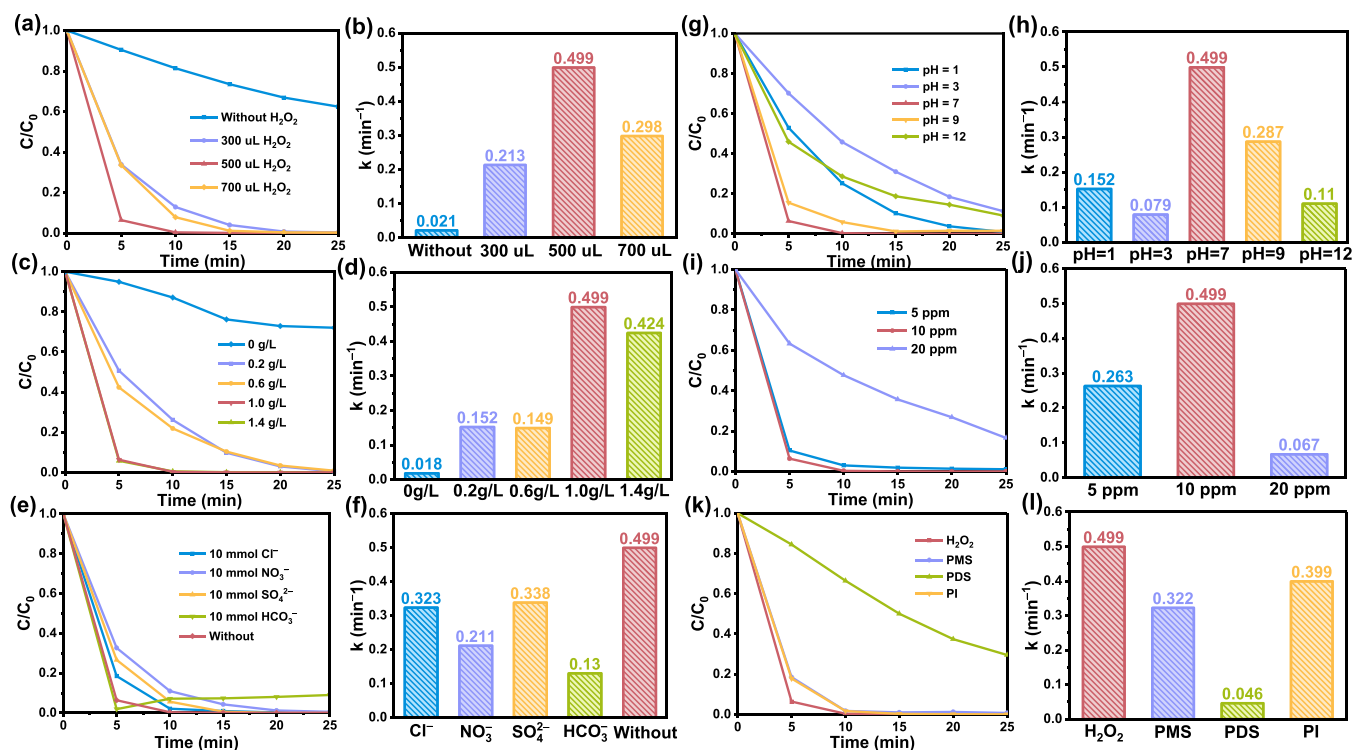
Fig. 6. Efficiency of photocatalytic degradation of ENR under different conditions of PCN/BFO-30: (a, b) H_2O_2 concentration, (c, d) photocatalyst dosage, (e, f) inorganic anions, (g, h) pH value, (i, j) ENR concentration and (k, l) oxidants.

to produce compound P1 and then oxidized to produce compound P2. P2 can continue to be converted to P3 by removing the aldehyde group, which was further transformed to P4 by losing the −NH group [53,54]. In pathway II, ENR is replaced by −OH under attack by •OH, cleavage and decarboxylation occur, and the quinolone groups are damaged by free radicals such as •O_2^- and h$^+$, resulting in P5 and P6. Through further oxidation, P7 is obtained [55]. In pathway III, the piperazine bond in ENR is substituted with −OH in aqueous solution to form P8. The active chemical then attacks the nitrogen atoms on the piperazine ring, causing the C−N bond to break, and the piperazine ring is subsequently oxidized to create P9. P9 can undergo oxidation of quinolones to form P10 [56–58]. The pathway compounds continue to crack to form P11 and P12, eventually producing small molecules such as CO_2 and H_2O.

In addition, the intermediate product toxicity of photocatalytic degradation of ENR by PCN/BFO composites was further evaluated by antibacterial experiments (Fig. 5b-c). *E. coli* is used as a reference bacterium. The number of *E. coli* in the medium was low due to the antibacterial properties of the antibiotics themselves (Fig. 5b). However, after photocatalytic degradation of ENR for 25 min, the number of *E. coli* on the medium increased significantly, almost covering the whole medium (Fig. 5c). The findings demonstrated that the intermediates of photocatalytic degradation of ENR by PCN/BFO samples were non-toxic or low toxic.

Fig. 6 illustrates the effect of different experimental conditions on the photocatalytic degradation efficiency of ENR. The influence of H_2O_2 concentration on the degradation system is depicted in Fig. 6a-b. The degrading efficiency of ENR rose dramatically when the volume of H_2O_2 was increased from 300 to 500 µL, and the associated k value improved from 0.213 min^{-1} to 0.499 min^{-1}. The reason is that more reactive oxygen species •OH are produced in the solution. However, the degrading performance of the catalyst was hindered and the corresponding rate constant was decreased to 0.298 min^{-1} when the volume of H_2O_2 was further raised to 700 µL. The reason for the decreased activity may be that the excess H_2O_2 captures •OH to generate HO$_2$•, which leads to •OH consumption [4]. The quantity of active sites is often

correlated with the photocatalyst dosage. Fig. 6c-d depicts the effect of varying photocatalyst dosage on ENR degradation. As the catalyst dosage increased from 0 g/L to 1.0 g/L, the corresponding reaction rate constant increased from 0.018 min^{-1} to 0.499 min^{-1}. The reason for this is that increasing the dosage of catalyst gives more reactive sites, which accelerates H_2O_2 consumption and the degradation of ENR [11]. However, the increasing dosage of catalyst cannot effectively improve the degradation efficiency. The result may be that the excess catalyst leads to aggregation and photo shielding, which leads to the reduction of the active site. The efficiency of the photo-Fenton process may be impacted by the high concentration of inorganic ions in natural water. Therefore, the effects of Cl$^-$, NO$_3^-$, SO$_4^{2-}$ and HCO$_3^-$ on the system were detected (Fig. 6e-f). In the presence of Cl$^-$, NO$_3^-$ and SO$_4^{2-}$, the rate of reaction constants decreases to 0.323 min^{-1}, 0.211 min^{-1} and 0.338 min^{-1}, respectively. The inhibitory effect of anion mainly comes from its quenching of active substance (Eqs. (1), (2) and (3)) [8,59]. Meanwhile, the degradation reaction can benefit from the buffering action of low concentration bicarbonate [60].

$$Cl^- + \bullet OH \rightarrow \bullet ClOH^- \tag{1}$$

$$NO_3^- + \bullet OH \rightarrow \bullet NO_3 + OH^- \tag{2}$$

$$SO_4^{2-} + h^+ \rightarrow \bullet SO_4^- \tag{3}$$

$$H_2O_2 \rightarrow H_2O + O_2 \tag{4}$$

The pH of the solution is another crucial variable in the photocatalytic degradation process. Fig. 6g-h shows the degradation activity in the pH range 1 − 12. The pseudo-first-order rate constant (k) is higher at pH = 7 (0.499 min^{-1}) than at other pH values. The experimental results show that the photocatalytic degradation process does not need to adjust pH, and can achieve the best activity under neutral conditions. The k value of PCN/BPO-30 degradation of ENR decreased to different degrees under acidic and alkaline conditions. However, the system still maintains a good pH suitability. The introduction of additional ions during pH adjustment may be responsible for the modest decrease in
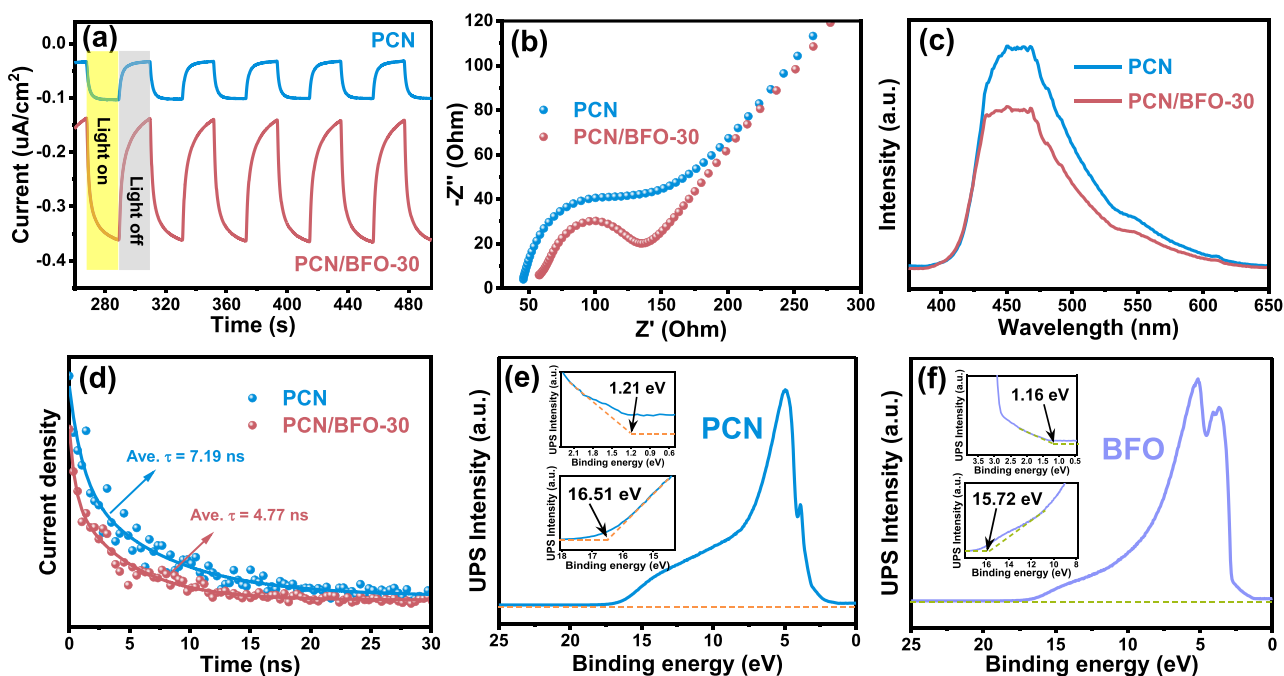
Fig. 7. (a) Transient photocurrent spectra, (b) EIS spectra, (c) PL spectra, and (d) TRPL spectra of PCN and PCN/BFO-30. UPS spectra of (e) PCN and (f) BFO.

reaction rate (Eq. (2)). Alkaline circumstances also lead to an increase in the inefficient decomposition of hydrogen peroxide (Eq. (4)), and the hydroxide in the solution combines with the active site to form a complex, which reduces the photo-Fenton reaction's effectiveness [8]. The effect of ENR concentration on photocatalytic degradation efficiency was discussed (Fig. 6i-j). Among them, the degradation rate of ENR solution with higher concentration decreased because more ENR intermediates competed for limited reactive oxygen species [61]. Moreover, in order to understand the synergic mechanism of different oxidants on photocatalysts, the commonly used oxidants peroxymonosulfate (PMS), persulfacte (PDS), periodate (PI) reported in the literature were added to the PCN/BFO photocatalytic system (Fig. 6k-l). The experimental results show that PCN/BFO photocatalysts can activate different oxidants under visible light. It is worth noting that although H_2O_2, PMS and PI can all achieve 100% enrofloxacin degradation efficiency, the degradation rate is the highest in the presence of H_2O_2 (0.499 min^{-1}). More importantly, using H_2O_2 as an oxidizer, its degradation process does not introduce impurities and the
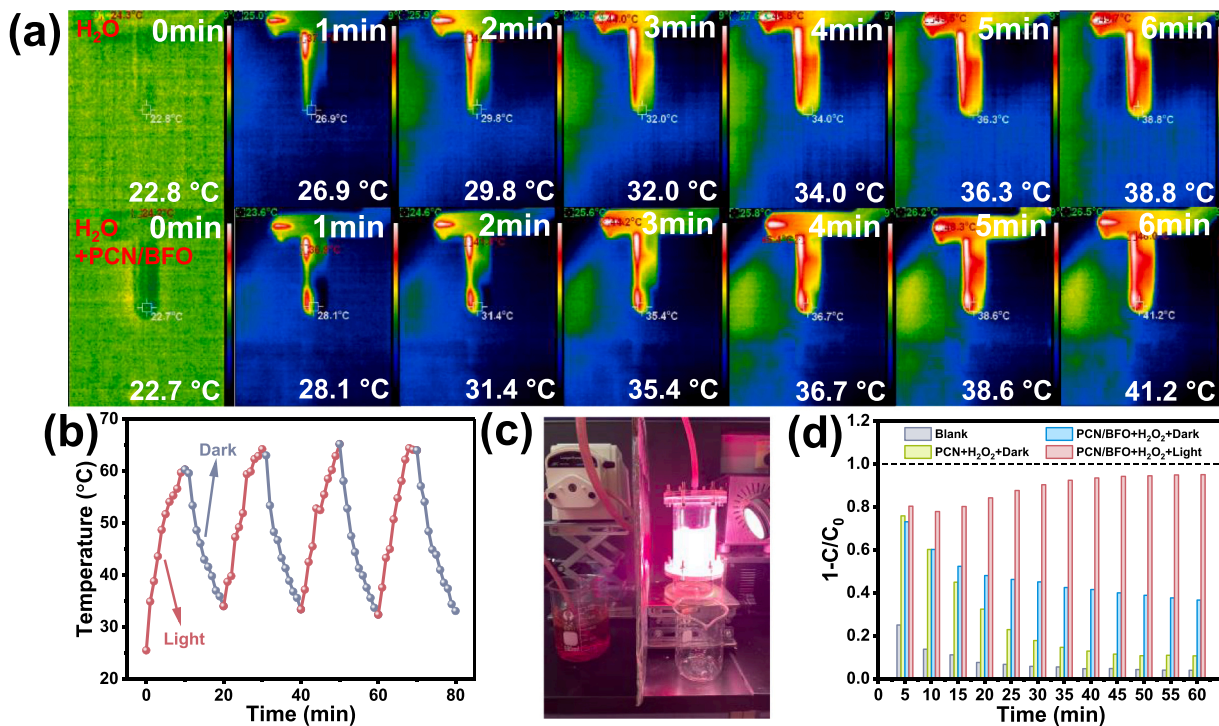

Fig. 8. (a) The IR images of photo-thermal effect for deionized water and PCN/BFO-30 in deionized water; (b) Photothermal stability diagram of PCN/BFO-30 in deionized water. (c) The photo-Fenton-like degradation of RhB reactor photograph; (d) The degradation efficiency of RhB in the obtained samples.
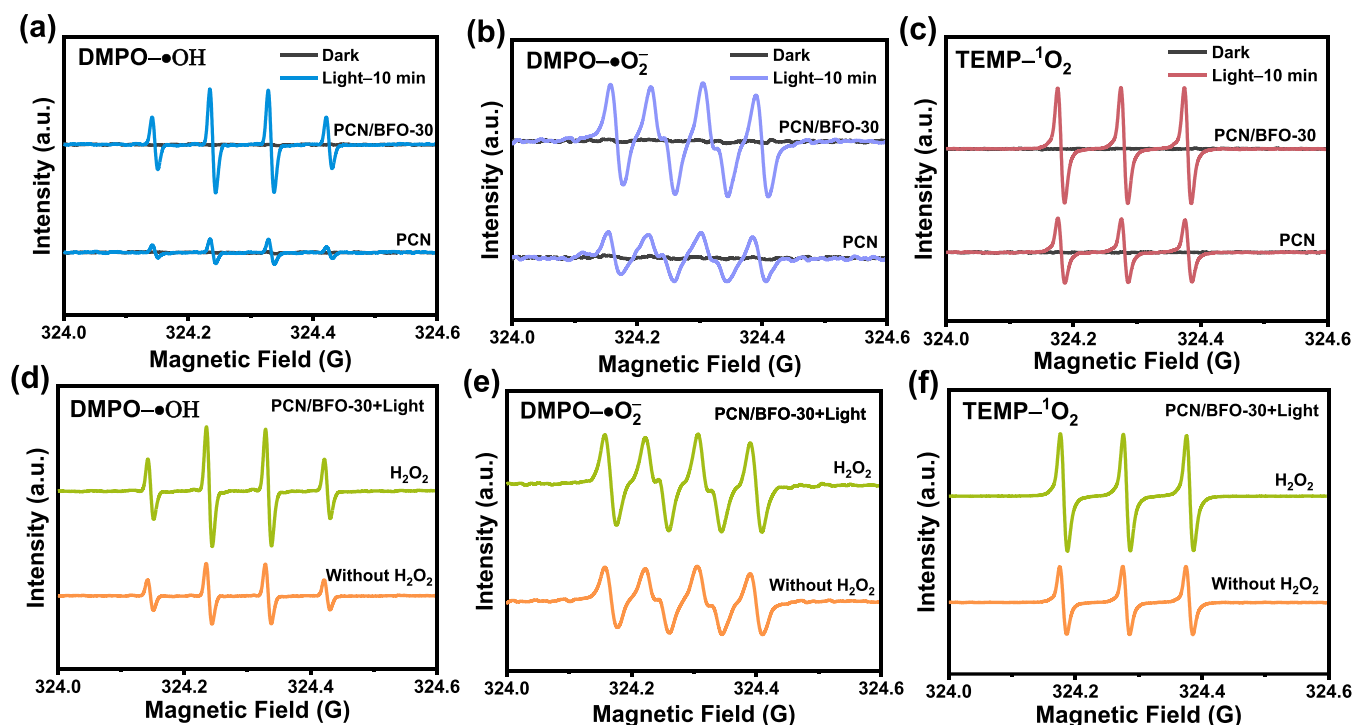
Fig. 9. ESR signals of (a, d) DMPO–•OH, (b, e) DMPO–•O_2^- and (c, f) TEMP–$^1O_2$ over PCN and PCN/BFO-30.

decomposition products are environmentally friendly. Therefore, the PCN-BFO/H_2O_2/vis system in this work shows great potential in practical applications.

3.3. Photocatalytic mechanism

The performance of photocatalyst is closely related to the separation, migration and recombination of photogenerated charges. The transient photocurrent response spectra of PCN and PCN/BFO-30 are displayed in Fig. 7a. The photocurrent intensity of PCN/BFO-30 is the highest, followed by PCN, indicating that PCN/BFO-30 exhibits a good photogenerated electron and hole separation rate. Fig. 7b shows the EIS spectra of the samples. The semi-arc radius of PCN/BFO-30 composite is the smallest, which indicates that it has the least charge transfer resistance and excellent charge transfer ability. Furthermore, the photoluminescence (PL) spectrum measured at the excitation wavelength of 337 nm is shown in Fig. 7c. The PL intensity of PCN is the highest, while the PL intensity of PCN/BFO in composites is relatively low. The results show that the N-defect composite may effectively prevent the $e^- – h^+$ recombination and improve the photocatalytic performance of the catalyst. TRPL spectroscopy was used to further analyze the photoinduced carrier transfer behavior and lifetime, as shown in Fig. 7d. PCN/BFO has a shorter carrier average PL lifetime (4.77 ns) compared to PCN (7.19 ns). The reason is that the PCN/BFO heterostructure creates a new electron transport channel. Therefore, the carrier transport rate is significantly improved and the photocatalytic activity is improved.

In order to obtain the band position of the sample more accurately, the PCN and BFO materials were tested using UPS technology. As can be seen from Fig. 7e-f, the cutoff energies (E_{cutoff}) of PCN and BFO were 16.51 and 15.72 eV, respectively, and the onset energies (E_{onset}) were 1.21 and 1.16 eV, respectively. The E_{VB} of PCN and BFO can be obtained by the following formula: E_{VB} (vs. vacuum) $= h\nu - (E_{cutoff} - E_{onset})$ [62], and E_{VB} (RHE) $= E_{VB}$ (vs. vacuum) $- 4.44$ eV, where $h\nu$ is 21.22 eV (the excitation energy of the He I source) [63]. The calculated E_{VB} of PCN and BFO are 1.48 and 2.22 eV, respectively. These E_{VB} results are similar to those obtained from empirical formulas. Furthermore, according to the formula $E_{CB} = E_{VB} - E_g$, the E_{CB} of PCN and BFO are calculated as -1.14

and 0.45 eV, respectively. In addition, the work functions (Φ) of PCN and BFO are calculated by the following formula: $\Phi = 21.22 - E_{cutoff}$ [62]. Therefore, the work functions of PCN and BFO are 4.71 and 5.5 eV, respectively, and the results are similar to those of DFT.

In order to explore the photothermal effect of photocatalyst in practical applications, the IR images of photocatalyst in water was further investigated. As shown in Fig. 8a, compared with the blank water sample, it is found that the photothermal temperature of the photocatalyst is higher than that of water at the same time. After 6 min of light, the surface temperature of the PCN/BFO-30 in deionized water can reach 41.2 °C. In addition, the photothermal cycling stability of the photocatalyst was also studied by switching lamp experiments (Fig. 8b). The PCN/BFO-30 photocatalyst maintained excellent photothermal stability (62 °C) after four cycles at a 10-minute light interval. It can be seen from the above experimental results that the PCN/BFO-30 photocatalyst still has good photothermal effect and cyclic stability in water.

In order to understand the potential of photocatalyst in practical application, a simple device for continuous degradation of pollutants was built (Fig. 8c). Taking Rhodamine B (RhB) as the model pollutant, 500 mL RhB solution (10 mg/L) containing 5 mL H_2O_2 (30 wt%) was prepared for the subsequent experiment. Adjust the rotational speed of the peristaltic pump to maintain the flow rate at 8 mL•min^{-1}, and the light source is provided by xenon lamp (> 400 nm). The 500 mg PCN/BFO-30 photocatalyst was adsorbed on the surface of polyvinylidene fluoride (PVDF) membrane by a vacuum filtration device for subsequent experiments (Fig. S5a). In contrast, the adsorption effect of PVDF membrane on RhB was investigated in the absence of photocatalyst (Fig. S5b). The efficiency of continuous degradation of RhB under different conditions is shown in Fig. 8d. The experimental results show that the adsorption of RhB by PVDF membrane is negligible. The PCN/BFO-30 showed the best photo-Fenton-like degradation activity of RhB, and the removal efficiency was close to 95% after 60 min. Similarly, PCN/BFO-30 also showed good degradation efficiency under dark-Fenton (40%), which was much higher than PCN (10%). It can be seen from the above experiments that the PCN/BFO-30 photocatalyst shows great potential in practical application.

DMPO and TEMP were used to determine the formation of active
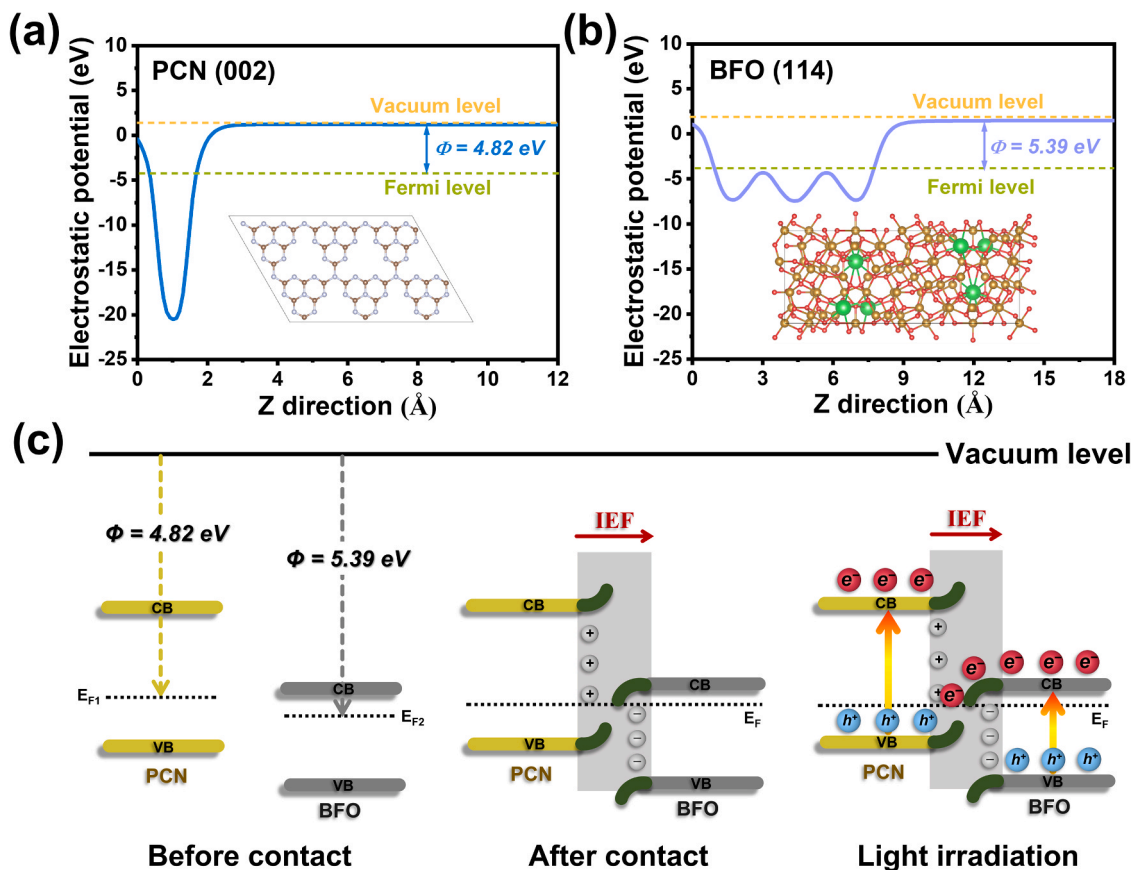
Fig. 10. Calculated work functions for (a) PCN (002) and (b) BFO (114) surfaces, respectively. (c) Band arrangement and charge transfer paths of PCN and BFO before contact, after dark contact and under light contact.

species, as can be seen in Fig. 9. DMPO− •OH, DMPO− •O$_2^-$, and TEMP−^{1}O$_2$ signals were not produced in the dark by PCN and PCN/BFO composites (Fig. 9a-c). However, PCN and PCN/BFO-30 have obvious peak signal under visible light irradiation, and the peak signal of composite material is stronger. The results showed that PCN/BFO-30 could produce more active species under visible light excitation. In addition, the signal peak of H$_2$O$_2$ added to the reaction system is displayed in Fig. 9d-f. The concentration of •OH, •O$_2^-$ and ^{1}O$_2$ increases when H$_2$O$_2$ is added to the reaction mixture, demonstrating the synergistic interaction between the Fenton reaction and visible light irradiation.

The work function (Φ) of the samples is computed using density functional theory (DFT) in order to further investigate the charge transfer direction at the interface of PCN and BFO. As indicated in Fig. 10a-b, the work functions of PCN and BFO are 4.82 and 5.39 eV, respectively, which corresponds to the higher Fermi level of PCN. Therefore, when PCN and BFO are tightly bound under dark conditions (Fig. 10c), the difference in Fermi levels causes the electrons of PCN to transfer into the BFO until the Fermi levels reach equilibrium [64]. This charge redistribution induces an internal electric field between the PCN and BFO, preventing the electrons of the PCN from continuously
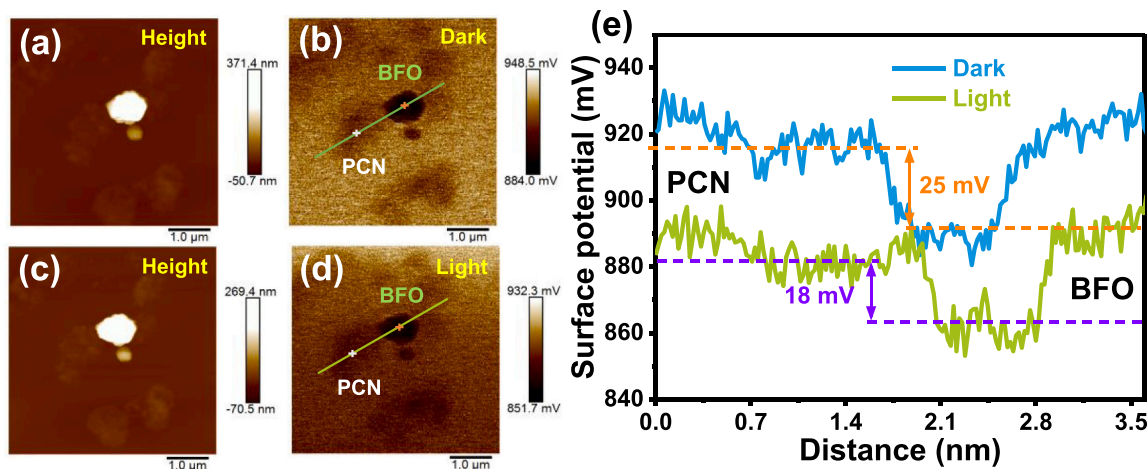
Fig. 11. (a, c) The pictures of KPFM height and (b, d) surface potential over the obtained PCN/BFO-30 photocatalyst in darkness and light, respectively. (e) Corresponding surface potential profiles.
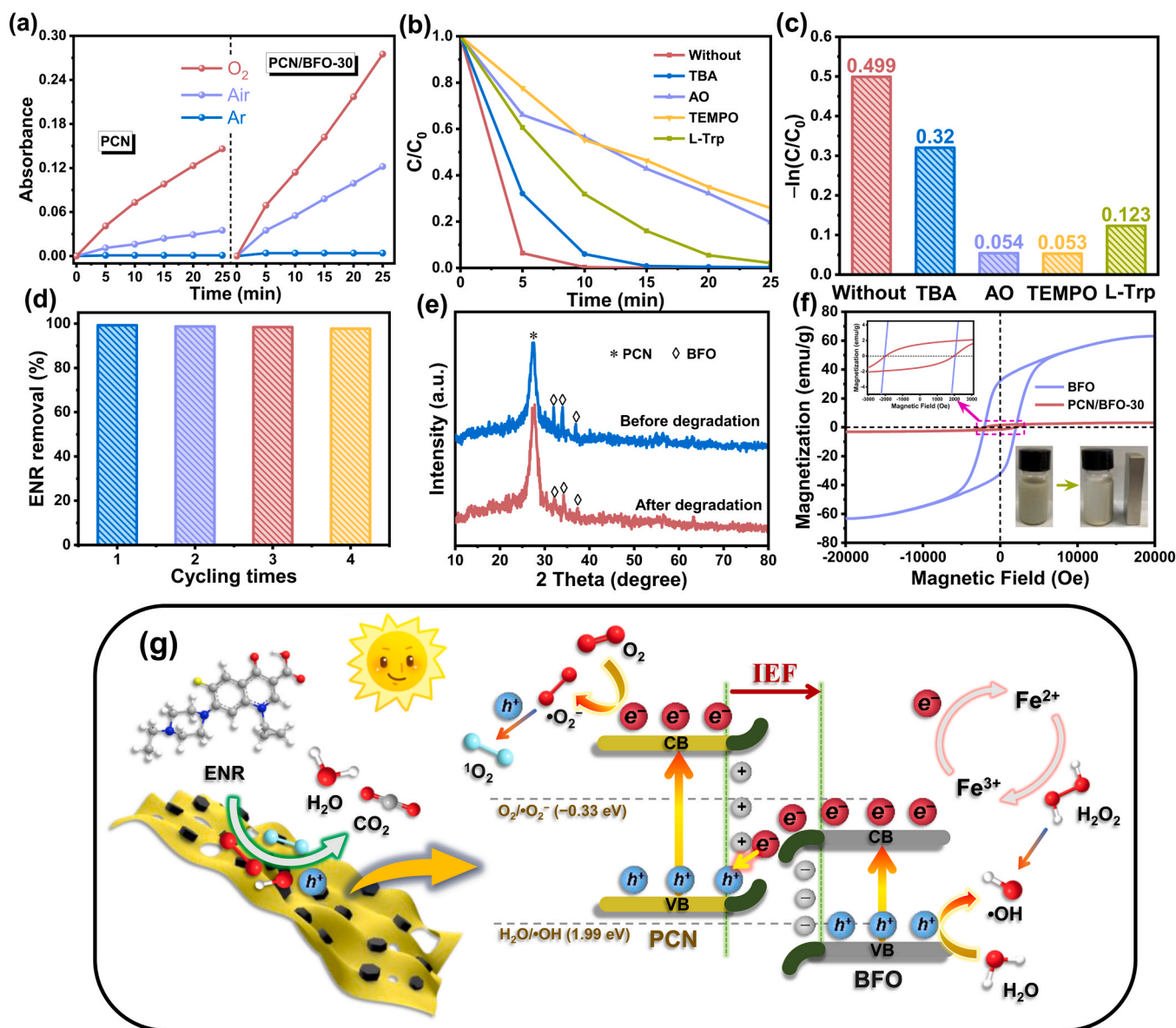
Fig. 12. (a) The product absorbance peak measured at 370 nm vs reaction time for PCN and PCN/BFO-30 under various gas conditions; (b, c) Trapping experiment and reaction rate constants of photocatalytic degradation system of PCN/BFO-30 composites; (d) The cycling experiments of PCN/BFO-30 and (e) XRD pattern of PCN/BFO-30 before and after photocatalytic degradation; (f) Magnetic hysteresis loop of BFO and PCN/BFO-30; (g) The possible mechanism over the S-scheme PCN/BFO heterojunction photo-Fenton to degrade enrofloxacin.

transferring the BFO. At the same time, PCN showed upward-curved band edges, while BFO showed downward-curved band edges. Furthermore, PCN and BFO are photoexcited under light conditions, which leads to the buildup of many electrons and holes in the bands of conduction and valence, respectively. Driven by the internal electric field, holes on PCN tend to recombine with electrons on BFO to form S-scheme transport paths. This process not only consumes useless electron holes and promotes the separation of photogenerated carriers, but also retains a significant proportion of carriers with strong redox properties.

In order to prove the results of DFT, the charge transfer path of PCN/BFO-30 internal electric field was thoroughly verified by Kelvin probe force microscopy (KPFM, Fig. 11). As can be seen from Fig. 11a and c, The morphology of composite materials is not significantly different before and after illumination. However, the surface potential varies significantly (Fig. 11b and d-e). In the dark environment, the surface potential difference between PCN and BFO is about 25 mV, and the potential of PCN is higher than that of BFO. The findings demonstrate

that internal electric field from PCN to BFO is formed in PCN/BFO-30 composites. In addition, the surface potentials of PCN and BFO were significantly reduced under light, indicating the accumulation of photogenerated e^- and h^+ [65–68]. Meanwhile, the surface potential difference between PCN and BFO is reduced to 18 mV. This result proves the electron transfer from PCN to BFO and further indicates the S-scheme transfer mechanism of charge carriers.

In order to illustrate the molecular oxygen activity of PCN/BFO modified with nitrogen vacancy, 3, 3′, 5, 5′- tetramethylbenzidine (TMB) was used as indicator molecule to explore its molecular oxygen activation activity (Fig. 12a). Moreover, the amount of O_2 activated by photocatalyst increases with the extension of light time. In addition, the oxidation rates of PCN and PCN/BPO-30 to TMB were significantly different in different gas atmospheres (Ar, Air, O_2), indicating that reactive oxygen species (ROS) were converted from oxygen. In order to further determine the mechanism of PCN/BFO degradation of ENR, the capture experiment of active species was carried out. TBA, AO, TEMPO and L-Trp were used as scavengers •OH, h^+, •O_2^-, and $^1O_2$, respectively

(Fig. 12b). Specifically, under the action of TBA, AO, TEMPO and L-Trp, PCN/BFO-30 photocatalytic degradation of ENR decreased from 0.499 min^{-1} to 0.320 min^{-1}, 0.054 min^{-1}, 0.053 min^{-1} and 0.053 min^{-1}, respectively (Fig. 12c). The experimental results further revealed the important role of h$^+$ and •O$_2^-$ radicals in the photocatalytic system. In order to further evaluate the stability of PCN/BFO-30 composites, the cyclic experiments of ENR degradation were carried out. The result is shown in Fig. 12d. The photocatalytic activity of PCN/BFO-30 did not significantly diminish after 4 cycles, showing that PCN/BFO-30 composites have high cyclic stability. In addition, XRD pattern of PCN/BFO catalyst before and after degradation was also analyzed, as illustrated in Fig. 12e. The main diffraction peak positions are essentially the same when compared to the XRD pattern of freshly synthesized PCN/BFO, further demonstrating the greater stability and reusability of the PCN/BFO-30 catalyst. The easy separation magnetization of photocatalyst is the basis of large-scale application. Therefore, the obtained sample was tested by vibrating sample magnetometer (VSM), as depicted in Fig. 12f. The saturation magnetization (Ms) values of BFO and PCN/BFO-30 samples were 63 and 3 emu/g, respectively. The reduced saturation magnetization in PCN/BFO-30 can still be collected by an external magnet (inset in Fig. 12f). In addition, the coercivity of PCN/BFO-30 showed little change compared to BFO, indicating that the structure of the magnetic material BFO did not change (inset in Fig. 12f). The research results reduce the practical application cost and provide the possibility of magnetic recovery.

Combining DRS energy band diagram (Fig. 3k), DFT calculation and KPFM, a possible S-scheme heterojunction structure (Fig. 12g) is proposed instead of p − n heterojunction, which is also proved by ESR results (Fig. 9). Specifically, under the excitation of visible light, the e$^-$ in VB of PCN and BFO migrate to CB respectively, forming e$^-$–h$^+$ pairs. Due to the interaction between PCN and BFO, the h$^+$ in the VB of PCN and the e$^-$ in the conduction band of BFO rapidly recombine. At the same time, the e$^-$ on the PCN/BFO composite are further trapped by the surface nitrogen defects of PCN and consumed by H$_2$O$_2$. The above e$^-$ migration path inhibits electron hole recombination. Then, since the conduction potential of PCN is more negative than E^0(O$_2$/•O$_2^-$) = −0.33 eV, the oxygen adsorbed by PCN can be reduced to •O$_2^-$ by electrons, and a portion of •O$_2^-$ is further oxidized to ^{1}O$_2$ by the holes. In addition, the VB potential of BFO is more positive than that of E^0(H$_2$O/•OH) = 1.99 eV, resulting in the h$^+$ oxidation of H$_2$O to •OH in solution. It should be noted that the cycle of Fe^{2+} and Fe^{3+} extends their service life at the same time. In summary, e$^-$ migration and the formation of active substances significantly promoted the activity of photocatalyst oxidation to degrade pollutants.

4. Conclusions

In summary, nitrogen defect PCN/BFO S-scheme heterojunction photocatalyst was prepared by simple grinding and calcination process. The results show that there is strong interfacial interaction between PCN and BFO, which enhances the separation effectiveness of e$^-$–h$^+$ pairs. Meanwhile, the construction of IEF and the formation of S-scheme heterojunction greatly enhanced the redox ability of PCN/BFO. The magnetic separation performance and photothermal effect of photocatalyst are due to the introduction of BFO. Photoelectric chemical test shows that the optimized PCN/BFO-30 materials have excellent e$^-$–h$^+$ pairs separation efficiency. Using ENR as the model pollutant, PCN/BFO-30 has excellent oxidation activity under photo-Fenton condition, and its degradation rate is 4 times that of pure PCN. In the meantime, the PCN/BFO-30 photo-Fenton system has a great ability to withstand anion interference and does not require the pH of the solution to be adjusted. In addition, the stability of PCN/BFO-30 was verified by cyclic experiments and related characterization. Compared with the original ENR solution, the biotoxicity after degradation was significantly reduced. The potential ENR degradation mechanism was deduced based on the experimental calculation and mass spectrometry analysis results. In conclusion, the PCN/BFO photo-Fenton system offers enormous promise for treating practical wastewater with antibiotics.

CRediT authorship contribution statement

Puyang Zhou: Methodology, Investigation, Writing – original draft. **Yan Wang:** Data curation. **Xiaorui Yan:** Data curation. **Yu Gan:** Data curation. **Changkun Xia:** Data curation. **Yuanguo Xu:** Supervision, Writing – review & editing, Funding acquisition. **Meng Xie:** Supervision, Writing – review & editing.

Declaration of Competing Interest

The authors declare that they have no known competing financial interests or personal relationships that could have appeared to influence the work reported in this paper.

Data Availability

No data was used for the research described in the article.

Appendix A. Supporting information

Supplementary data associated with this article can be found in the online version at doi:10.1016/j.apcatb.2023.123485.

References

[1] J.J. Li, X.W. Cheng, H.X. Zhang, J.F. Gou, X.Y. Zhang, D. Wu, D.D. Dionysiou, Insights into performance and mechanism of ZnO/CuCo$_2$O$_4$ composite as heterogeneous photoactivator of peroxymonosulfate for enrofloxacin degradation, J. Hazard. Mater. 448 (2023), 130946.

[2] Y.-X. Li, W.-L. Duan, B.-Y. Ren, J. Luan, F. Guo, Facile synthesis of Fe-doped Zn-based coordination polymer composite with enhanced visible-light-driven activity for degradation of multiple antibiotics, Sep. Purif. Technol. 311 (2023), 123337.

[3] P. S.-Molina, P. P.-Bolaños, A. Lorenzo, A. Agüera, J.L. García Sánchez, S. Malato, J.A. Sánchez Pérez, Assessment of solar raceway pond reactors for removal of contaminants of emerging concern by photo-Fenton at circumneutral pH from very different municipal wastewater effluents, Chem. Eng. J. 366 (2019) 141–149.

[4] X.F. Li, X.L. Shen, Y.L. Qiu, Z.L. Zhu, H. Zhang, D.Q. Yin, Fe$_3$O$_4$ quantum dots mediated P-g-C$_3$N$_4$/BiOI as an efficient and recyclable Z-scheme photo-Fenton catalyst for tetracycline degradation and bacterial inactivation, J. Hazard. Mater. 456 (2023), 131677.

[5] G. Yang, Y.J. Liang, H. Zheng, X.R. Zhang, J. Jia, Fe-polyoxometalate nanodots decorated Bi$_2$MoO$_6$ nanosheets with dominant {010} facets for photo-Fenton degradation of antibiotics over a wide pH range: Mechanism insight and toxicity assessment, Sep. Purif. Technol. 310 (2023), 123167.

[6] N. Thomas, D.D. Dionysiou, S.C. Pillai, Heterogeneous Fenton catalysts: a review of recent advances, J. Hazard. Mater. 404 (2021), 124082.

[7] C.H. Liu, H.L. Dai, C.Q. Tan, Q.Y. Pan, F.P. Hu, X.M. Peng, Photo-Fenton degradation of tetracycline over Z-scheme Fe-g-C$_3$N$_4$/Bi$_2$WO$_6$ heterojunctions: Mechanism insight, degradation pathways and DFT calculation, Appl. Catal. B: Environ. 310 (2022), 121326.

[8] C. Lai, D.S. Ma, H. Yi, M.M. Zhang, F.H. Xu, X.Q. Huo, H.Y. Ye, L. Li, L. Yang, L. Tang, M. Yan, Functional partition of Fe and Ti co-doped g-C$_3$N$_4$ for photo-Fenton degradation of oxytetracycline: Performance, mechanism, and DFT study, Sep. Purif. Technol. 306 (2023), 122546.

[9] Y. Zhang, X. Chen, M.-S. Cui, Z. Guo, Y.-H. Chen, K.-P. Cui, Z.-G. Ding, R. Weerasooriya, Binding Fe-doped g-C$_3$N$_4$ on the porous diatomite for efficient degradation of tetracycline via photo-Fenton process, J. Environ. Chem. Eng. 10 (2022), 107406.

[10] C.M. Li, N. Su, H.H. Wu, C.B. Liu, G.B. Che, H.J. Dong, Synergies of adjacent sites in atomically dispersed ruthenium toward achieving stable hydrogen evolution, Inorg. Chem. 61 (2022) 13453–13461.

[11] X. Zhang, B. Ren, X. Li, B.M. Liu, S.W. Wang, P. Yu, Y.H. Xu, G.Q. Jiang, High-efficiency removal of tetracycline by carbon-bridge-doped g-C$_3$N$_4$/Fe$_3$O$_4$ magnetic heterogeneous catalyst through photo-Fenton process, J. Hazard. Mater. 418 (2021), 126333.

[12] C.-X. Xu, Y.-L. Kong, W.-J. Zhang, M.-D. Yang, K. Wang, L. Chang, W. Chen, G.-B. Huang, J. Zhang, S-scheme 2D/2D FeTiO₃/g-C₃N₄ hybrid architectures as visible-light-driven photo-Fenton catalysts for tetracycline hydrochloride degradation, Sep. Purif. Technol. 303 (2022), 122266.

[13] Z.Q. Cao, D. Sun, H. Hu, W.X. Li, Z.Y. Xiong, M.F. He, S.Q. Cai, Y. Fan, L.L. Zheng, S.F. Kang, FeC₂O₄/g-C₃N₄ self-assemble nanorods regulate stimuli-responsive ferroptosis via photo-fenton mechanism, Appl. Surf. Sci. 611 (2023), 155671.

[14] J.J. Jiang, X.Y. Wang, Y. Liu, Y.H. Ma, T.R. Li, Y.H. Lin, T.F. Xie, S.S. Dong, Photo-Fenton degradation of emerging pollutants over Fe-POM nanoparticle/porous and ultrathin g-C₃N₄ nanosheet with rich nitrogen defect: Degradation mechanism, pathways, and products toxicity assessment, Appl. Catal. B: Environ. 278 (2020), 119349.

[15] X.Y. Zhan, Y.X. Zeng, H. Zhang, X.Q. Wang, D.F. Jin, H.X. Jin, S.L. Luo, L.M. Yang, B. Hong, The coral-like carbon nitride array: rational design for efficient photodegradation of tetracycline under visible light, J. Environ. Chem. Eng. 11 (2023), 109201.

[16] D.D. Wei, J.Q. Wu, Y.F. Wang, J.P. Zhong, D.G. Li, X.Y. Jin, Y.L. Wu, P. Chen, H.J. Liu, W.Y. Lv, G.G. Liu, Dual defect sites of nitrogen vacancy and cyano group synergistically boost the activation of oxygen molecules for efficient photocatalytic decontamination, Chem. Eng. J. 462 (2023), 142291.

[17] Q.Q. Zhang, A.C. Zhang, H.G. Zhang, X. Zhang, H.X. Li, Z.Q. Tan, F.M. Meng, H.X. Deng, Z.J. Sun, Enhanced photocatalytic Hg⁰ removal over Z-scheme CeO₂/Bi₂O₇I nanorod composite under fluorescent light irradiation, Atmos. Pollut. Res. 13 (2022), 101542.

[18] Y.W. Liu, A.C. Zhang, Q.Q. Zhang, Y.Y. Mei, C.K. Wang, Y.X. Wang, J. Xiang, S. Su, X.M. Zhang, Z.Q. Tan, Facile synthesis of ternary AgBr/BiOI/Bi₂O₂CO₃ heterostructures via BiOI self-sacrifice for efficient photocatalytic removal of gaseous mercury, Sep. Purif. Technol. 299 (2022), 121722.

[19] M. Dai, H.J. Yu, W.H. Chen, K.Y.-A. Qu, D. Zhai, C.C. Liu, S. Zhao, S.G. Wang, Z.L. He, Boosting photocatalytic activity of CdLa₂S₄/ZnIn₂S₄ S-scheme heterojunctions with spatial separation of photoexcited carries, Chem. Eng. J. 470 (2023), 144240.

[20] Y.H. Su, X.Y. Xu, R. Li, X. Luo, H.J. Yao, S.C. Fang, K.P. Homewood, Z.B. Huang, Y. Gao, X.X. Chen, Design and fabrication of a CdS QDs/Bi₂WO₆ monolayer S-scheme heterojunction configuration for highly efficient photocatalytic degradation of trace ethylene in air, Chem. Eng. J. 429 (2022), 132241.

[21] S.J. Li, C.C. Wang, M.J. Cai, F. Yang, Y.P. Liu, J.L. Chen, P. Zhang, X. Li, X.B. Chen, Facile fabrication of TaON/Bi₂MoO₆ core–shell S-scheme heterojunction nanofibers for boosting visible-light catalytic levofloxacin degradation and Cr(VI) reduction, Chem. Eng. J. 428 (2022), 131158.

[22] S.S. Wu, X. Yu, J.L. Zhang, Y.M. Zhang, Y. Zhu, M.S. Zhu, Construction of BiOCl/CuBi₂O₄ S-scheme heterojunction with oxygen vacancy for enhanced photocatalytic diclofenac degradation and nitric oxide removal, Chem. Eng. J. 411 (2021), 128555.

[23] K. Dou, C.Y. Peng, R.C. Wang, H.P. Cao, C. Yao, J.F. Qiu, J.L. Liu, N. Tsidaev, W. Wang, S-scheme tubular g-C₃N₄/BiOI heterojunctions for boosting photodegradation of tetracycline and Cr(VI): Mechanism insight, degradation pathway and DFT calculation, Chem. Eng. J. 455 (2023), 140813.

[24] L. Rifai, F. Fattouh, K. Habanjar, N. Yaacoub, R. Awad, Exchange spring behaviour in BaFe₁₂O₁₉/CoFe₂O₄ magnetic nanocomposites, J. Alloy. Compd. 868 (2021), 159072.

[25] M.Q. Wang, Y. Lin, H.B. Yang, Y. Qiu, S. Wang, A novel plate-like BaFe₁₂O₁₉@MoS₂ core-shell structure composite with excellent microwave absorbing properties, J. Alloy. Compd. 817 (2020), 153265.

[26] M. Xie, D.D. Wang, L.Q. Jing, W. Wei, Y.G. Xu, H. Xu, H.M. Li, J.M. Xie, Preparation of magnetically recoverable and Z-scheme BaFe₁₂O₁₉/AgBr composite for degradation of 2-Mercaptobenzothiazole and Methyl orange under visible light, Appl. Surf. Sci. 521 (2020), 146343.

[27] S. Feng, T.P. Xie, J.K. Wang, J.W. Yang, D.S. Kong, C.W. Liu, S.L. Chen, F.L. Yang, M.J. Pan, J. Yang, H.G. Du, H.Y. Chen, Photocatalytic activation of PMS over magnetic heterojunction photocatalyst SrTiO₃/BaFe₁₂O₁₉ for tetracycline ultrafast degradation, Chem. Eng. J. 470 (2023), 143900.

[28] H.F. Wang, Y.G. Xu, L.Q. Jing, S.Q. Huang, Y. Zhao, M.Q. He, H. Xu, H.M. Li, Novel magnetic BaFe₁₂O₁₉/g-C₃N₄ composites with enhanced thermocatalytic and photo-Fenton activity under visible-light, J. Alloy. Compd. 710 (2017) 510–518.

[29] P.Y. Zhou, F. Chen, X.M. Su, T.T. Zhang, S.C. Meng, M. Xie, Y.H. Song, X.R. Yan, Y.G. Xu, Ag₂O modified magnetic BaFe₁₂O₁₉/C₃N₄ photocatalysts with enhanced antibiotic removal: Photocatalytic mechanism and toxicity evaluation, Adv. Powder Technol. 34 (2023), 104015.

[30] R.D. Tang, H. Zeng, Y.C. Deng, S. Xiong, L. Li, Z.P. Zhou, J.J. Wang, L. Tang, Dual modulation on peroxymonosulfate activation site and photocarrier separation in carbon nitride for efficient photocatalytic organics degradation: Efficacy and mechanism evaluation, Appl. Catal. B: Environ. 336 (2023), 122918.

[31] F. Li, T.B. Huang, F.B. Sun, L. Chen, P.S. Li, F. Shao, X.D. Yang, W. Liu, Ferric oxide nanoclusters with low-spin Feᴵᴵᴵ anchored g-C₃N₄ rod for boosting photocatalytic activity and degradation of diclofenac in water under solar light, Appl. Catal. B: Environ. 317 (2022), 121725.

[32] Z.Z. Zhang, R. Ji, Q.M. Sun, J.H. He, D.Y. Chen, N.J. Li, H. Li, A. Marcomini, Q.F. Xu, J.M. Lu, Enhanced photocatalytic degradation of 2-chlorophenol over Z-scheme heterojunction of CdS-decorated oxygen-doped g-C₃N₄ under visible-light, Appl. Catal. B: Environ. 324 (2023), 122276.

[33] Y.C. Cao, G.Q. Yuan, Y. Guo, X.L. Hu, G.Z. Fang, S. Wang, Facile synthesis of TiO₂/g-C₃N₄ nanosheet heterojunctions for efficient photocatalytic degradation of tartrazine under simulated sunlight, Appl. Surf. Sci. 600 (2022), 154169.

[34] D.K. Gorai, S.K. Kuila, A. Kumar, Md.I. Ahmad, T.K. Kundu, Insight into the effect of Li/P co-doping on the electronic structure and photocatalytic performance of g-C₃N₄ by the first principle, Appl. Surf. Sci. 623 (2023), 157031.

[35] X.H. Wang, X.H. Wang, W.L. Tian, A.L. Meng, Z.J. Li, S.X. Li, L. Wang, G.C. Li, High-energy ball-milling constructing P-doped g-C₃N₄/MoP heterojunction with Mo–N bond bridged interface and Schottky barrier for enhanced photocatalytic H2 evolution, Appl. Catal. B: Environ. 303 (2022), 120933.

[36] J.P. Liang, L. Fu, K. Gao, P. Zhang, X.G. Duan, X.B. Gong, L. Cai, Accelerated sulfate radical generation from peroxymonosulfate by ZIF-67-derived Co₃O₄ encapsulated in g-C₃N₄: a gift from in situ growth, Chem. Eng. J. 460 (2023), 141797.

[37] N. Ali, A. Zada, M. Zahid, A. Ismail, M. Rafiq, A. Riaz, A. Khan, Enhanced photodegradation of methylene blue with alkaline and transition-metal ferrite nanophotocatalysts under direct sun light irradiation, J. Chin. Chem. Soc. 66 (2019) 402–408.

[38] L.X. Wang, J. Zhang, Q.T. Zhang, N.C. Xu, J. Song, XAFS and XPS studies on site occupation of Sm³⁺ ions in Sm doped M-type BaFe₁₂O₁₉, J. Magn. Magn. Mater. 377 (2015) 362–367.

[39] M.C. Zhang, X.Y. Chen, Z.Y. Chen, R.H. Dan, Y.X. Wei, H.H. Rong, Q. Wang, X. Chen, A.Z. Han, Y. Wang, W.J. Shao, H. Zhang, Y.R. Zhang, L. Wang, J.G. Xu, Y. Tong, Exploration of threshold and resistive-switching behaviors in MXene/BaFe₁₂O₁₉ ferroelectric memristors, Appl. Surf. Sci. 613 (2023), 155956.

[40] J.N. Li, J.H. Huang, G.M. Zeng, C.Y. Zhang, H.B. Yu, Q.F. Wan, K.X. Yi, W. Zhang, H.L. Pang, S. Liu, S.Z. Li, W.J. He, Efficient photosynthesis of H₂O₂ via two-electron oxygen reduction reaction by defective g-C₃N₄ with terminal cyano groups and nitrogen vacancies, Chem. Eng. J. 463 (2023), 142512.

[41] Y.Z. Wu, W.Q. Zhou, L. Zhou, S.-I. In, J.Y. Lei, L.Z. Wang, J.L. Zhang, Y.D. Liu, , Near-infrared photothermal effect enhanced heterogeneous catalysis of Co₃O₄/PDA composite for highly efficient activation of peroxymonosulfate to degrade antibiotic pollutants, Chem. Eng. J. 474 (2023), 145267.

[42] K.Y. Chen, Y.X. Shi, P. Shu, Z.Y. Luo, W.L. Shi, F. Guo, Construction of core–shell FeS₂@ZnIn₂S₄ hollow hierarchical structure S-scheme heterojunction for boosted photothermal-assisted photocatalytic H₂ production, Chem. Eng. J. 454 (2023), 140053.

[43] C.C. Yang, Y.J. Gung, W.C. Hung, T.H. Ting, K.H. Wu, Infrared and microwave absorbing properties of BaTiO₃/polyaniline and BaFe₁₂O₁₉/polyaniline composites, Compos. Sci. Technol. 70 (2010) 466–471.

[44] K.M. Qi, Z.R. Wang, X.Y. Xie, Z.W. Wang, Photocatalytic performance of pyrochar and hydrochar in heterojunction photocatalyst for organic pollutants degradation: Activity comparison and mechanism insight, Chem. Eng. J. 467 (2023), 143424.

[45] V.K. Parida, S.K. Srivastava, S. Chowdhury, A.K. Gupta, Facile synthesis of 2D/0D Bi₂O₃/MnO₂ Z-scheme heterojunction for enhanced visible light-assisted photocatalytic degradation of acetaminophen, Chem. Eng. J. 472 (2023), 144969.

[46] A. Gordanshekan, S. Arabian, A.R.S. Nazar, M. Farhadian, S. Tangestaninejad, A comprehensive comparison of green Bi₂WO₆/g-C₃N₄ and Bi₂WO₆/TiO₂ S-scheme heterojunctions for photocatalytic adsorption/degradation of Cefixime: Artificial neural network, degradation pathway, and toxicity estimation, Chem. Eng. J. 451 (2023), 139067.

[47] C.K. Wang, A.C. Zhang, D. Peng, Y.Y. Mei, Y.X. Wang, J. Guo, Z.Q. Tan, Y.W. Liu, H.X. Li, Facile fabrication of 3D spherical Ag₂WO₄ doped BiOI/BiOCl double S-scheme heterojunction photocatalyst with efficient activity for mercury removal, J. Environ. Chem. Eng. 10 (2022), 108517.

[48] S.Y. Ji, Y.L. Yang, Z.W. Zhou, X. Li, Y.K. Liu, Photocatalysis-Fenton of Fe-doped g-C₃N₄ catalyst and its excellent degradation performance towards RhB, J. Water Process Eng. 40 (2021), 101804.

[49] X.H. He, L.L. Wang, S.M. Sun, X.C. Yang, H.Y. Tian, Z.J. Xia, X.L. Li, X.L. Yan, X.J. Pu, Z. Jiao, Self-assembled synthesis of recyclable g-C₃N₄/NH₂-MIL-53(Fe) aerogel for enhanced photocatalytic degradation of organic pollutants, J. Alloy. Compd. 946 (2023), 169391.

[50] S. Shu, H.J. Wang, X.Y. Guo, Y. Wang, X.L. Zeng, Efficient photocatalytic degradation of sulfamethazine by Cu-CuₓO/TiO₂ composites: Performance, photocatalytic mechanism and degradation pathways, Sep. Purif. Technol. 323 (2023), 124458.

[51] J. Xiong, X.B. Li, J.T. Huang, X.M. Gao, Z. Chen, J.Y. Liu, H. Lia, B.B. Kang, W.Q. Yao, Y.F. Zhu, CN/rGO@BPQDs high-low junctions with stretching spatial charge separation ability for photocatalytic degradation and H₂O₂ production, Appl. Catal. B: Environ. 266 (2020) 118.

[52] G.L. Puma, A. Brucato, Dimensionless analysis of slurry photocatalytic reactors using two-flux and six-flux radiation absorption–scattering models, Catal. Today 122 (2007) 78–90.

[53] B. Qi, T.T. Chen, T.F. Zhang, R.X. Jiang, W.M. Zhang, X.C. Li, A novel continuous all-weather photo-electric synergistic treatment system for refractory organic compounds and its application in degrading enrofloxacin, Chemosphere 329 (2023), 138632.

[54] J.X. Huang, D.G. Li, R.B. Li, P. Chen, Q.X. Zhang, H.J. Liu, W.Y. Lv, G.G. Liu, Y.P. Feng, One-step synthesis of phosphorus/oxygen co-doped g-C₃N₄/anatase TiO₂ Z-scheme photocatalyst for significantly enhanced visible-light photocatalysis degradation of enrofloxacin, J. Hazard. Mater. 386 (2020), 121634.

[55] T.C. Li, J.X. Liu, F. Shi, H.Y. Zhang, H.J. Zhang, C.C. Ma, M. Wasim, A novel S-type CsₓWO₃/BiOI heterojunction photocatalyst constructed in graphene aerogel with high degradation efficiency for enrofloxacin: Degradation mechanism and DFT calculation, J. Environ. Chem. Eng. 11 (2023), 109301.

[56] Y. Wei, G.L. Lu, D.R. Xie, T.Y. Sun, Y. Liu, Y. Zhang, J.T. An, M.H. Li, H. Guo, Degradation of enrofloxacin in aqueous by DBD plasma and UV: Degradation performance, mechanism and toxicity assessment, Chem. Eng. J. 431 (2022), 133360.

[57] X.Y. Zhang, W.B. Liu, Y.R. Zhou, Y.H. Li, Y. Yang, J.F. Gou, J.W. Shang, X. W. Cheng, Photo-assisted bismuth ferrite/manganese dioxide/nickel foam composites activating PMS for degradation of enrofloxacin in water, Sep. Purif. Technol. 301 (2022), 121988.

[58] R.J. Du, P. Chen, Q.X. Zhang, G. Yu, The degradation of enrofloxacin by a non-metallic heptazine-based OCN polymer: Kinetics, mechanism and effect of water constituents, Chemosphere 273 (2021) 128435.

[59] A. Kumar, K. Sharma, M. Thakur, D. Pathania, A. Sharma, Fabrication of high visible light active $LaFeO_3/Cl-g-C_3N_4/RGO$ heterojunction for solar assisted photo-degradation of aceclofenac, J. Environ. Chem. Eng. 10 (2022), 108098.

[60] J. Ren, L.S. Jiang, Y. Li, G.K. Zhang, Cobalt doped bismuth oxysulfide with abundant oxygen vacancies towards tetracycline degradation through peroxymonosulfate activation, Sep. Purif. Technol. 275 (2021), 119100.

[61] H.R. Sun, F. Guo, J.J. Pan, W. Huang, K. Wang, W.L. Shi, One-pot thermal polymerization route to prepare N-deficient modified $g-C_3N_4$ for the degradation of tetracycline by the synergistic effect of photocatalysis and persulfate-based advanced oxidation process, Chem. Eng. J. 406 (2021), 126844.

[62] M.L. Sheng, C. Gan, Y. Li, Z.J. Hu, Q. Zhou, L. Qin, J.M. Ren, H.Y. Jiang, Photocatalytic C-O activation and biomass derived polymer precursor production with CO_2 over redox centers spatially separated $Sv-ZnIn_2S_4/BiVO_4$, Appl. Catal. B: Environ. 339 (2023), 123138.

[63] R.J. Yang, Q.Q. Chen, Y.Y. Ma, R.S. Zhu, Y.Y. Fan, J.Y. Huang, H.N. Niu, Y. Dong, D. Li, Y.F. Zhang, L. Mei, B.Y. Chen, Z.Y. Zeng, Highly efficient photocatalytic hydrogen evolution and simultaneous formaldehyde degradation over Z-scheme $ZnIn_2S_4-NiO/BiVO_4$ hierarchical heterojunction under visible light irradiation, Chem. Eng. J. 423 (2021), 130164.

[64] S.J. Li, C.C. Wang, Y.P. Liu, Y.Z. Liu, M.J. Cai, W. Zhao, X.G. Duan, S-scheme MIL-101(Fe) octahedrons modified Bi_2WO_6 microspheres for photocatalytic decontamination of Cr(VI) and tetracycline hydrochloride: Synergistic insights, reaction pathways, and toxicity analysis, Chem. Eng. J. 455 (2023), 140943.

[65] R.J. Chen, H.T. Yin, L. Wang, Z.Q. Zhang, J. Ding, J.F. Zhang, H. Wan, G.F. Guan, Enwrapping $g-C_3N_4$ on In_2O_3 hollow hexagonal tubular for photocatalytic CO_2 conversion: construction, characterization, and Z-scheme mechanism insight, J. Colloid Interface Sci. 631 (2023) 122–132.

[66] H. Wang, H.F. Zhang, J.H. Wang, Y.Y. Gao, F.T. Fan, K.F. Wu, X. Zong, C. Li, Mechanistic understanding of efficient photocatalytic H_2 evolution on two-dimensional layered lead iodide hybrid perovskites, Angew. Chem. Int. Ed. 60 (2021) 7376–7381.

[67] Y. Jiang, H.-Y. Chen, J.-Y. Li, J.-F. Liao, H.-H. Zhang, X.-D. Wang, D.-B. Kuang, Z-Scheme 2D/2D heterojunction of $CsPbBr_3/Bi_2WO_6$ for improved photocatalytic CO_2 reduction, Adv. Funct. Mater. 30 (2020), 2004293.

[68] H. Zhao, L.R. Wang, G.H. Liu, Y.T. Liu, S.Q. Zhang, L.H. Wang, X.B. Zheng, L. Y. Zhou, J. Gao, J.F. Shi, Y.J. Jiang, Hollow Rh-COF@COF S-scheme heterojunction for photocatalytic nicotinamide cofactor regeneration, ACS Catal. 13 (2023) 6619–6629.